

## Accelerated Article Preview

# COVID-19 tissue atlases reveal SARS-CoV-2 pathology and cellular targets

Received: 16 November 2020

Accepted: 19 April 2021

Accelerated Article Preview

Published online 29 April 2021

Cite this article as: Delorey, T. M. et al. COVID-19 tissue atlases reveal SARS-CoV-2 pathology and cellular targets. *Nature* <https://doi.org/10.1038/s41586-021-03570-8> (2021).

Toni M. Delorey, Carly G. K. Ziegler, Graham Heimberg, Rachelly Normand, Yiming Yang, Åsa Segerstolpe, Domenic Abbondanza, Stephen J. Fleming, Ayshwarya Subramanian, Daniel T. Montoro, Karthik A. Jagadeesh, Kushal K. Dey, Pritha Sen, Michal Slyper, Yered H. Pita-Juárez, Devan Phillips, Jana Biermann, Zohar Bloom-Ackermann, Nick Barkas, Andrea Ganna, James Gomez, Johannes C. Melms, Igor Katsyv, Erica Normandin, Pourya Naderi, Yury V. Popov, Siddharth S. Raju, Sebastian Niezen, Linus T.-Y. Tsai, Katherine J. Siddle, Malika Sud, Victoria M. Tran, Shamsudheen K. Vellarikkal, Yiping Wang, Liat Amir-Zilberstein, Deepak S. Atri, Joseph Beechem, Olga R. Brook, Jonathan Chen, Prajan Divakar, Phylcia Dorceus, Jesse M. Engreitz, Adam Essene, Donna M. Fitzgerald, Robin Fropf, Steven Gazal, Joshua Gould, John Grzyb, Tyler Harvey, Jonathan Hecht, Tyler Hether, Judit Jané-Valbuena, Michael Leney-Greene, Hui Ma, Cristin McCabe, Daniel E. McLoughlin, Eric M. Miller, Christoph Muus, Mari Niemi, Robert Padera, Liuliu Pan, Deepti Pant, Carmel Pe'er, Jenna Pfiffner-Borges, Christopher J. Pinto, Jacob Plaisted, Jason Reeves, Marty Ross, Melissa Rudy, Erroll H. Rueckert, Michelle Siciliano, Alexander Sturm, Ellen Todres, Avinash Waghray, Sarah Warren, Shuting Zhang, Daniel R. Zollinger, Lisa Cosimi, Rajat M. Gupta, Nir Hacohen, Hanina Hibshoosh, Winston Hide, Alkes L. Price, Jayaraj Rajagopal, Purushothama Rao Tata, Stefan Riedel, Gyongyi Szabo, Timothy L. Tickle, Patrick T. Ellinor, Deborah Hung, Pardis C. Sabeti, Richard Novak, Robert Rogers, Donald E. Ingber, Z. Gordon Jiang, Dejan Juric, Mehrtash Babadi, Samouil L. Farhi, Benjamin Izar, James R. Stone, Ioannis S. Vlachos, Isaac H. Solomon, Orr Ashenberg, Caroline B. M. Porter, Bo Li, Alex K. Shalek, Alexandra-Chloé Villani, Orit Rozenblatt-Rosen & Aviv Regev

This is a PDF file of a peer-reviewed paper that has been accepted for publication. Although unedited, the content has been subjected to preliminary formatting. Nature is providing this early version of the typeset paper as a service to our authors and readers. The text and figures will undergo copyediting and a proof review before the paper is published in its final form. Please note that during the production process errors may be discovered which could affect the content, and all legal disclaimers apply.

# COVID-19 tissue atlases reveal SARS-CoV-2 pathology and cellular targets

<https://doi.org/10.1038/s41586-021-03570-8>

Received: 16 November 2020

Accepted: 19 April 2021

Published online: 29 April 2021

Toni M. Delorey<sup>1,6,4</sup>, Carly G. K. Ziegler<sup>2,3,4,5,6,7,6,4</sup>, Graham Heimberg<sup>1,6,4</sup>, Rachelly Normand<sup>2,8,9,10,11,6,4</sup>, Yiming Yang<sup>1,8,6,4</sup>, Åsa Segerstolpe<sup>1,6,4</sup>, Domenic Abbondanza<sup>1,2,6,4</sup>, Stephen J. Fleming<sup>12,13,6,4</sup>, Ayshwarya Subramanian<sup>1,6,4</sup>, Daniel T. Montoro<sup>2,6,4</sup>, Karthik A. Jagadeesh<sup>1,6,4</sup>, Kushal K. Dey<sup>14,6,4</sup>, Pritha Sen<sup>2,8,15,16,6,4</sup>, Michal Slyper<sup>1,6,4</sup>, Yered H. Pita-Juárez<sup>2,10,17,18,19,6,4</sup>, Devan Phillips<sup>1,6,4</sup>, Jana Biermann<sup>20,21,6,4</sup>, Zohar Bloom-Ackermann<sup>22</sup>, Nick Barkas<sup>12</sup>, Andrea Ganna<sup>23,24</sup>, James Gomez<sup>22</sup>, Johannes C. Melms<sup>20,21</sup>, Igor Katsyov<sup>25</sup>, Erica Normandin<sup>2,10</sup>, Pourya Naderi<sup>10,17,18</sup>, Yury V. Popov<sup>10,26,27</sup>, Siddharth S. Raju<sup>2,28,29</sup>, Sebastian Niezen<sup>10,26,27</sup>, Linus T.-Y. Tsai<sup>2,10,26,30,31</sup>, Katherine J. Siddle<sup>2,32</sup>, Malika Sud<sup>1</sup>, Victoria M. Tran<sup>22</sup>, Shamsudheen K. Vellarikkal<sup>2,33</sup>, Yiping Wang<sup>20,21</sup>, Liat Amir-Zilberstein<sup>1</sup>, Deepak S. Atri<sup>2,33</sup>, Joseph Beechem<sup>34</sup>, Olga R. Brook<sup>35</sup>, Jonathan Chen<sup>2,36</sup>, Prajan Divakar<sup>34</sup>, Phylcia Dorceus<sup>1</sup>, Jesse M. Engreitz<sup>2,37</sup>, Adam Essene<sup>26,30,31</sup>, Donna M. Fitzgerald<sup>38</sup>, Robin Fropf<sup>34</sup>, Steven Gazal<sup>39</sup>, Joshua Gould<sup>12</sup>, John Grzyb<sup>40</sup>, Tyler Harvey<sup>1</sup>, Jonathan Hecht<sup>10,17</sup>, Tyler Hether<sup>34</sup>, Judit Jané-Valbuena<sup>1</sup>, Michael Leney-Greene<sup>2</sup>, Hui Ma<sup>1,8</sup>, Cristin McCabe<sup>1</sup>, Daniel E. McLoughlin<sup>38</sup>, Eric M. Miller<sup>34</sup>, Christoph Muus<sup>2,41</sup>, Mari Niemi<sup>23</sup>, Robert Padera<sup>40,42,43</sup>, Liuliu Pan<sup>34</sup>, Deepti Pant<sup>26,30,31</sup>, Carmel Pe'er<sup>1</sup>, Jenna Pfflner-Borges<sup>2</sup>, Christopher J. Pinto<sup>16,38</sup>, Jacob Plaisted<sup>40</sup>, Jason Reeves<sup>34</sup>, Marty Ross<sup>34</sup>, Melissa Rudy<sup>2</sup>, Erroll H. Rueckert<sup>34</sup>, Michelle Siciliano<sup>40</sup>, Alexander Sturm<sup>22</sup>, Ellen Todres<sup>1</sup>, Avinash Waghray<sup>44,45</sup>, Sarah Warren<sup>34</sup>, Shuting Zhang<sup>22</sup>, Daniel R. Zollinger<sup>34</sup>, Lisa Cosimi<sup>46</sup>, Rajat M. Gupta<sup>2,33</sup>, Nir Hacohen<sup>2,9,47</sup>, Hanina Hibshoosh<sup>25</sup>, Winston Hide<sup>10,17,18,19</sup>, Alkes L. Price<sup>14</sup>, Jayaraj Rajagopal<sup>38</sup>, Purushothama Rao Tata<sup>48</sup>, Stefan Riedel<sup>10,17</sup>, Gyongyi Szabo<sup>2,10,26</sup>, Timothy L. Tickle<sup>1,12</sup>, Patrick T. Ellinor<sup>49,65</sup>, Deborah Hung<sup>22,50,51,65</sup>, Pardis C. Sabeti<sup>2,32,52,53,54,65</sup>, Richard Novak<sup>55,65</sup>, Robert Rogers<sup>26,56,65</sup>, Donald E. Ingber<sup>41,55,57,65</sup>, Z. Gordon Jiang<sup>10,26,27,65</sup>, Dejan Juric<sup>16,38,65</sup>, Mehrtash Babadi<sup>12,13,65</sup>, Samouil L. Farhi<sup>1,2,65</sup>, Benjamin Izar<sup>20,21,58,59,65</sup>, James R. Stone<sup>36,65</sup>, Ioannis S. Vlachos<sup>2,10,17,18,19,65</sup>, Isaac H. Solomon<sup>40,65</sup>, Orr Ashenberg<sup>1,65</sup>, Caroline B. M. Porter<sup>1,65</sup>, Bo Li<sup>1,8,16,65</sup>, Alex K. Shalek<sup>2,3,4,5,6,7,10,44,60,61,62,65</sup>, Alexandra-Chloé Villani<sup>2,8,9,16,65</sup>, Orit Rozenblatt-Rosen<sup>1,63,65</sup> & Aviv Regev<sup>1,5,53,63,65</sup>

COVID-19, caused by SARS-CoV-2, can result in acute respiratory distress syndrome and multiple-organ failure<sup>1–4</sup>, but little is known about its pathophysiology. Here, we generated single-cell atlases of 23 lung, 16 kidney, 16 liver and 19 heart COVID-19 autopsy donor tissue samples, and spatial atlases of 14 lung donors. Integrated computational analysis uncovered substantial remodeling in the lung epithelial, immune and stromal compartments, with evidence of multiple paths of failed tissue regeneration, including defective alveolar type 2 differentiation and expansion of fibroblasts and putative TP63<sup>+</sup> intrapulmonary basal-like progenitor cells. Viral RNAs were enriched in mononuclear phagocytic and endothelial lung cells which induced specific host programs. Spatial analysis in lung distinguished inflammatory host responses in lung regions with and without viral RNA. Analysis of the other tissue atlases showed transcriptional alterations in multiple cell types in COVID-19 donor heart tissue, and mapped cell types and genes implicated with disease severity based on COVID-19 GWAS. Our foundational dataset elucidates the biological impact of severe SARS-CoV-2 infection across the body, a key step towards new treatments.

The host response to severe acute respiratory syndrome coronavirus 2 (SARS-CoV-2) infection ranges from asymptomatic infection to severe coronavirus disease 2019 (COVID-19) and death. The leading cause of mortality is acute lung injury and acute respiratory distress syndrome (ARDS), or direct complications with multiple organ failure<sup>1–4</sup>. Clinical deterioration in acute illness leads to ineffective viral clearance and collateral tissue damage<sup>1–5</sup>. Severe COVID-19 is also accompanied by an

inappropriate pro-inflammatory host immune response and a diminished antiviral interferon response<sup>6–8</sup>.

Many molecular and cellular questions related to COVID-19 pathophysiology remain unanswered, including: how cell compositions and gene programs shift; which cells are infected; and, how associated genetic loci drive disease. Autopsies are critical to understanding severe COVID-19 pathophysiology<sup>9–12</sup>, but comprehensive

genomic studies are challenged by long post mortem intervals (PMI).

Here, we developed a large cross-body COVID-19 autopsy biobank of 420 autopsy specimens, spanning 11 organs and used it to generate a single cell atlas of COVID-19 lung, kidney, liver and heart and a lung spatial atlas, in a subset of 14–18 donors per organ. Our atlases provide critical insights into the pathogenesis of severe COVID-19.

## A COVID-19 autopsy cohort and biobank

We assembled an autopsy cohort of eleven male and six female donors, of different ages (>30–>89yo), racial/ethnic backgrounds, intermittent mandatory ventilation (IMV; 0–24 days) periods and days from symptom start (S/s) to death (Fig. 1a, Supplementary Information Table 1). From most donors, we collected at least lung, heart, and liver tissue (Fig. 1a, Extended Data Fig. 1a, Methods), preserving specimens for single cell and spatial analysis. We optimized single cell and single nucleus RNA-seq (sc/snRNA-Seq) protocols for Biosafety Level 3, and NanoString GeoMx workflows to spatially profile RNA from different tissue compartment by cell composition or viral RNA (Methods).

## COVID-19 cell atlases

We generated sc/snRNA-Seq atlases of lung ( $n=16$  donors,  $k=106,792$  cells/nuclei,  $m=23$  specimens; Donors D1–8,10–17), heart ( $n=18$ ,  $k=40,880$ ,  $m=19$ , D1–8,10–11,14–17, 27–28,31–32), liver ( $n=15$ ,  $k=47,001$ ,  $m=16$ ; D1–7,10–17) and kidney ( $n=16$ ,  $k=33,872$ ,  $m=16$ ; D4–8,10–12,14–15,17,25–26,28–30). While initial tests showed some differences in cell type proportions between snRNA-Seq and scRNA-Seq, snRNA-Seq performed better overall<sup>13</sup> (Extended Data Fig. 1b–d and *data not shown*) and was used for the remaining samples.

We developed a computational pipeline (Fig. 1b) to tackle unique technical challenges. We used CellBender remove-background<sup>14</sup> to remove ambient RNA, enhancing cell distinction and marker specificity (Extended Data Fig. 1e–h; Methods); we rapidly quality controlled, pre-processed, and batch corrected data with cloud-based Cumulus<sup>15</sup> (Extended Data Fig. 2a–g, Methods); and we automatically annotated cells/nuclei by transferring labels from previous atlases (Fig. 2a, Extended Data Fig. 2h, Methods). We refined these labels with manual annotation of sub-clusters in each main lineage (Fig. 2b, Extended Data Fig. 2i–2n, Methods). The former allowed us to compare to other data resources (without clustering or batch correction); the latter to refine cell identity assignments with detailed domain knowledge.

## A cell census of the COVID-19 lung

Automatic annotation defined 28 subsets of parenchymal, endothelial and immune cells (Fig. 2a, Supplementary Information Table 2, Methods), with further manual annotation within subgroupings (Fig. 2b, Extended Data Fig. 2.4, Methods). Deconvolution of bulk RNA-Seq from the same samples largely agreed (Extended Data Fig. 3a,b, Methods), and our two annotation strategies had 94% agreement (Extended Data Fig. 3c–e).

Among immune cells we distinguished: six cell myeloid subsets:  $CD14^{\text{high}}CD16^{\text{high}}$  inflammatory monocytes with antimicrobial properties, and five macrophage subsets (Extended Data Fig. 2j, 4b) enriched for scavenger receptors, toll-like receptor ligands, inflammatory transcriptional regulators, or metabolism genes; four B and plasma cell subsets:  $BLIMP-1^{\text{high}}$  plasma cells<sup>16,17</sup>;  $BLIMP-1^{\text{intermediate}}$  plasma cells; B cells; and,  $JCHAIN$ -expressing plasmablasts (Extended Data Fig. 2k, 4b); five T and NK subsets: two  $CD4^+$  subsets, including  $T_{\text{regs}}$  and a metabolically active subset; one  $CD8^+$  subset; and two T/NK cell subsets (Extended Data Fig. 2l, 4b), including one with cytotoxic effector genes. The dearth of neutrophils (Fig. 2a, 419 cells) is likely due to freezing or limitations of droplet-based sc/snRNA-seq<sup>13</sup>.

We identified seven endothelial subsets (Extended Data Fig. 2m, 4b)<sup>18,19</sup>: arterial; venous and lymphatic; capillary aerocytes; capillary EC-1; and capillary EC-2 and a mixed subset (Methods), and three stromal subsets: fibroblasts; proliferative fibroblasts; and myofibroblasts<sup>19</sup> (Extended Data Fig. 2n, Supplementary Information Table 3).

There were eight epithelial subsets including: club/secretory cells; AT1 cells; AT2 cells; and proliferative AT2 cells (Fig. 2b). One subset corresponded to a previously described AT2 to AT1 transitional cell state ( $KRT8^+$  pre-alveolar type (PATS) 1 transitional cell state (PATS/ADI/DATP)<sup>20–22</sup> (Fig. 2b).

## Changes in lung cell composition

Compared to normal lung from a matching region (Fig. 2c, Methods), AT2 cells were significantly decreased ( $FDR=2.8 \times 10^{-15}$ , Dirichlet multinomial regression, Methods), possibly reflecting virally-induced cell death<sup>23–25</sup>. Dendritic cells ( $FDR=0.004$ ), macrophages ( $FDR=3.6 \times 10^{-10}$ ), NK cells ( $FDR=0.018$ ), fibroblasts ( $FDR=0.013$ ), lymphatic endothelial cells ( $FDR=0.00058$ ), and vascular endothelial cells ( $FDR=0.00011$ ) all increased.

Cell proportions varied between donors (Extended Data Fig. 5a–b). While variation was not significantly correlated to PMI, age, or sex, IMV was positively correlated with epithelial cell fraction ( $FDR=0.007$ ; Spearman  $\rho=0.765$ ) and negatively with T and NK cell fraction ( $FDR=0.041$ ;  $\rho=-0.62$ ). Fewer days on a ventilator may indicate a rapidly deteriorating condition. This is corroborated by the nominally significant positive correlation between epithelial cell fraction and S/s to death ( $\rho=0.671$ ,  $p\text{-value}=0.004$ , but  $FDR=0.053$ ).

## Induced programs in epithelial cells

There were widespread, cell type specific, transcriptional changes in lung cell types in COVID-19 (Extended Data Fig. 5c, Methods), most notably in  $CD16^+$  monocytes (1,580 upregulated genes), lymphatic endothelial (578), vascular endothelial (317), AT2 (309), and AT1 (307) cells. Within AT2 cells, there was higher expression ( $p<0.0004$ ) of genes associated with host viral response (Fig. 2d), including programmed cell death ( $STAT1$ ), inflammation and adaptive immune response (Supplementary Information Table 4). Lung surfactant genes were downregulated, consistent with *in vitro* reports<sup>21</sup>.

## Failed paths for AT1 cell regeneration

The PATS program signature was increased in COVID-19 pneumocytes ( $p\text{-value}<2.2 \times 10^{-16}$ , one-sided Mann–Whitney U test) (Fig. 2e, Extended Data Fig. 5d). This progenitor program is induced during lung injury<sup>20–22</sup> (e.g., idiopathic pulmonary fibrosis), consistent with fibrosis in severe COVID-19<sup>26,27</sup>. These studies also highlight fibroblast expansion, which we also observe (Fig. 2c).

A subset of PATS program cells, distinct from  $KRT5^+/TP63^+$  airway basal cells, expressed canonical ( $KRT8/CLDN4/CDKN1A$ ) and non-canonical ( $KRT5/TP63/KRT17$ ) PATS markers (Fig. 2f, Extended Data Fig. 5d, Supplementary Information Table 3). These may be  $TP63^+$  intrapulmonary basal-like progenitor cells (IPBLP), identified in H1N1 influenza mouse models<sup>28</sup> and act as an emergency cellular reserve for severely damaged alveoli<sup>29</sup>. The putative IPBLP cells express interferon viral-defense and progenitor cell differentiation genes (Supplementary Information Table 3). Thus, multiple emergency pathways for alveolar cell regeneration are activated in lung (Fig. 2g, Discussion).

## Changed cell composition with viral load

To determine viral load and associated host responses, we analyzed donor and cell type-specific distributions of SARS-CoV-2 reads (Fig. 3a, b, Extended Data Fig. 6a–d, Methods). Reads spanned the entire SARS-CoV-2 genome, with bias toward positive-sense alignments.

A few cells had reads aligning to all viral segments, including the negative strand (Extended Data Fig. 6e), potentially indicating productive infection. Viral detection was not technically driven (Extended Data Fig. 6f-i), and inter-donor variation was consistent with SARS-CoV-2 qRT-PCR on bulk RNA (Extended Data Fig. 6j-l, Methods). Viral load was negatively correlated with S/s to death (Fig. 3c), as previously reported<sup>30,31</sup>. Bulk RNA-Seq yielded nine unique complete viral genomes from nine donors with high viral loads (Extended Data Fig. 6m, Methods); all genomes carried the D614G allele. We identified no other common respiratory viral co-infections (Extended Data Fig. 6n). Total viral burden per sample (including ambient RNA, Methods) positively correlated with proportions of mast cells, specific macrophage subsets, venular endothelial cells, and capillary aerocytes' endothelial cells (Extended Data Fig. 6o-u).

Genes upregulated in biopsies with high *vs.* low/no viral load (Methods) included viral response and innate immune processes ( $\log_2FC > 1.4$ , Wald test, FDR-corrected p-value  $< 0.05$ , Extended Data Fig. 6v, Supplementary Information Table 4) and significantly overlapped with those in bulk RNA-Seq of other studies of post-mortem COVID-19 lungs (FDR =  $3.12 \times 10^{-6}$ , Kolmogorov-Smirnov test)<sup>32</sup>. Down-regulated genes ( $\log_2FC < -1.4$ , Wald test, FDR-corrected p-value  $< 0.05$ ) were involved in surfactant metabolism dysfunction and lamellar bodies (secretory vesicles in AT2 cells<sup>33</sup>).

### Lung cells enriched for SARS-CoV-2 RNA

Myeloid cells were the cell category most enriched for SARS-CoV-2 RNA (158 cells following correction for ambient RNA, FDR  $< 0.012$ , Fig. 3a, Extended Data Fig. 6w-y, Methods), with particular enrichment in  $CD14^{high}CD16^{high}$  inflammatory monocytes (FDR  $< 0.005$ ) and  $LDB2^{high}OSMR^{high}YAP1^{high}$  macrophages (FDR  $< 0.02$ , Extended Data Fig. 6x, 7a,b), although enrichment scores in individual donors varied. There was elevated, but non-significantly enriched, viral RNA in endothelial cells, with the capillary 2 endothelial cells (cluster 3, FDR  $< 0.017$ ) and lymphatic endothelial cells (cluster 7, FDR  $< 0.006$ ) enriched compared to other endothelial subsets (Fig. 3a, Extended Data Fig. 6w,y, 7c,d). There were also SARS-CoV-2+ cells among mast cells, and B and plasma cells, and viral RNA reads in multiple other cell types (Fig. 3a, Extended Data Fig. 6w). Notably, SARS-CoV-2+ cells did not co-express the entry factors *ACE2* and *TMPRSS2*, or other hypothesized entry cofactors (Fig. 3b, Extended Data Fig. 7e-h).

### Immune programs in SARS-CoV-2+ cells

SARS-CoV-2+ cells had distinct transcriptional programs compared to RNA- counterparts, with differentially expressed genes (FDR  $< 0.05$ ; Methods) in epithelial and myeloid cells, including  $PPARG^{high}CD151^{high}$  macrophages and  $CD14^{high}CD16^{high}$  inflammatory monocytes (Supplementary Information Table 5). Genes upregulated in epithelial SARS-CoV-2+ cells were enriched for TNF, API and chemokine/cytokine signaling, SARS-CoV-2 driven cell responses *in vitro*<sup>32</sup>, and keratinization pathways, which may reflect injury response (Extended Data Fig. 7i). Genes upregulated in myeloid SARS-CoV-2+ cells were enriched for chemokine and cytokine signaling, and responses to interferon, TNF, intracellular pathogens, and viruses (Fig. 3d Extended Data Fig. 7j-m, Supplementary Information Table 5), as previously described<sup>34,35</sup>. Cytokines and viral host response genes were upregulated in both  $CD14^{high}CD16^{high}$  inflammatory monocytes and  $PPARG^{high}CD151^{high}$  macrophages (Extended Data Fig. 7m, Supplementary Information Table 5), including *CXCL10* and *CXCL11*, which were upregulated in NP swabs<sup>35</sup> and bronchoalveolar lavages<sup>34</sup>.

### A spatial atlas of COVID-19 lung

To provide tissue context, we used Nanostring GeoMx Digital Spatial Profiling (DSP) for transcriptomic profiling from regions of

interest (ROIs) (Methods) in 14 donors, including three healthy donors (Extended Data Fig. 1a). ROIs spanned a range of anatomical structures and viral abundance based on SARS-CoV-2 RNA hybridization signals; when possible, we segmented them to PanCK<sup>+</sup> and PanCK<sup>-</sup>, and inflamed and normal-appearing alveoli areas of illumination (AOIs) to capture RNA (Fig. 4a, Extended Data Fig. 8a, Extended Data Fig. 9a, Methods). We acquired high quality profiles (Extended Data Fig. 8b) from matched AOIs based on distance to morphological landmarks (Methods). SARS-CoV-2 RNA expression varied by donor, with elevated levels in four donors (Extended Data Fig. 8c,d, Methods), consistent with viral qRT-PCR and sc/snRNA-Seq. Given the good agreement between a targeted 1,811 gene panel and a whole transcriptome (WTA) panel (18,335 genes) (Extended Data Fig. 8e-g, Supplementary Information Table 6), we focused our analyses on WTA data. For D8-12, 18-24, we contrasted COVID-19 and healthy donors and COVID-19 epithelial and non-epithelial AOIs; for D13-17, we focused on distinct anatomical regions and inflamed *vs.* normal-appearing regions within donors.

### Inflammatory activation in alveoli

Deconvolution of major cell type composition (Fig. 4b, Extended Data Fig. 8h, Supplementary Information Table 7-8, Methods) showed inferred AT1 and AT2 cells dominating the PanCK<sup>+</sup> compartments and greater cellular diversity in the PanCK<sup>-</sup> compartment. COVID-19 PanCK<sup>+</sup> AOIs had increased fibroblast and myofibroblast scores compared to controls, in line with parallel spatial studies<sup>36,37</sup>.

Comparing COVID-19 alveolar AOIs *vs.* control lungs from deceased healthy donors ("healthy"), there was up-regulation of interferon- $\alpha$  and  $\gamma$  response genes and oxidative phosphorylation pathways (Fig. 4c, Extended Data Fig. 8i-k, Supplementary Information Table 6), similar to bulk RNA-Seq of highly infected tissue (*IFIT1, IFIT3, IDO1, GZMB, LAG3, NKG7, PRF1*) and to SARS-CoV-2+ myeloid cells (*TNFAIP6, CXCL11, CCL8, ISG1, GBP5*), and consistent with PANoptosis in a COVID-19 model<sup>38</sup>. Conversely, TNF $\alpha$ , IL2-STAT5, and TGF $\beta$  signaling as well as apical junction and hypoxia were downregulated. Decreased TNF  $\alpha$  signaling expression in PanCK<sup>+</sup> alveoli contrasts with its increase in SARS-CoV-2+ epithelial cells in snRNA-seq and with reported<sup>38</sup> synergy between TNF  $\alpha$  and IFN $\gamma$  in COVID-19 mouse models.

Comparing inflamed and normal-appearing AOIs within the same alveolar biopsies of COVID-19 lungs (Extended Data Fig. 9, Supplementary Information Table 9, D13-D17), upregulated genes were enriched for innate immune and inflammatory pathways<sup>39,40</sup>, including neutrophil degranulation (FDR =  $5.2 \times 10^{-17}$ ) and IFN $\gamma$  (FDR =  $3.4 \times 10^{-15}$ ) and interleukin (FDR =  $1.4 \times 10^{-13}$ ) signaling. TNF pathway expression was elevated in inflamed tissue albeit not significantly (FDR = 0.097). Claudins and tight junction pathways were downregulated, corroborating a disrupted alveolar barrier, as in influenza<sup>41,42</sup>. Cilium assembly genes were enriched when comparing bronchial epithelial AOIs and matched normal-appearing alveoli (Extended Data Fig. 9d, Supplementary Information Table 9).

Comparing SARS-CoV-2 high and low AOIs (Fig. 4d, e, Extended Data Fig. 8l,m, Methods) revealed induction of the viral *ORF1ab* and S genes and upregulation of chemokines (*CXCL2, CXCL3*) and immediate early genes in the PanCK<sup>+</sup> compartment, consistent with snRNA-Seq (Supplementary Information Table 9, Extended Data Fig. 7i). *NT5C*, encoding a nucleotidase with a preference for 5'-dNTPs, is consistently upregulated in SARS-CoV-2 high AOIs (Fig. 4e, Extended Data Fig. 8m, Supplementary Information Table 9). This gene is not known to play a role in lung injury and should be further studied.

### COVID-19 impact on heart, kidney, liver

We next profiled liver, heart, and kidney by snRNA-Seq with automated and manual annotation of parenchymal, endothelial and immune cells (Methods, Extended Data Fig. 10, 11). Although other studies have

reported viral reads in COVID-19 non-lung tissues<sup>43</sup>, we detected very few viral RNA reads in all three tissues, most of which could not be assigned to nuclei (Extended Data Fig. 11l); this absence was confirmed by NanoString DSP and RNAscope (*data not shown*).

Focusing on heart, both cell composition and gene programs changed between COVID-19 and healthy heart. There was a significant reduction in the proportion of cardiomyocytes and pericytes, and an increase in vascular endothelial cells (Extended Data Fig. 11e). Genes upregulated (FDR < 0.01) in cardiomyocytes, pericytes, or fibroblasts (Extended Data Fig. 11g-i, Supplementary Information Table 10) included *PLCG2*, whose cardiac role is unknown but was induced in all major heart cell subtypes (Extended Data Fig. 11j), and *AFDN*, upregulated in endothelial cells (Extended Data Fig. 11k), which encodes a junction adherens complex component<sup>44</sup> necessary for endothelial barrier function. Upregulated pathways include oxidative stress-induced apoptosis in pericytes, cell adhesion and immune pathways in cardiomyocytes, and cell differentiation processes in fibroblasts (Supplementary Information Table 10).

### COVID-19 cell types related through GWAS

Finally, we aimed to identify genes and cell types associated with COVID-19 risk by integrating our atlas data with GWAS<sup>45</sup> for common<sup>46</sup> variants associated with COVID-19 (Methods). Among 26 genes proximal to six COVID-19 GWAS regions (Supplementary Information Table 11, Methods), 14 genes had higher average expression in the lung (p-value < 0.05, t-test; Extended Data Fig. 12a-d), 21 had significant (FDR < 0.05) expression specificity in at least one lung cell type, including *FOXP4* (chr 6, AT1 and AT2 cells), and *CCR1* and *CCRL2* (chr 3, macrophages) (Extended Data Fig. 12e, Supplementary Information Table 11), and 18 were differentially expressed (FDR < 0.05) in COVID-19 vs. healthy lung (e.g., *SLC6A20* in goblet cells, *CCR5* in CD8 T cells and T<sub>regs</sub>, and *CCR1* in macrophage and CD16 monocytes, (Extended Data Fig. 12f, Supplementary Information Table 11).

We related heritability from GWAS of COVID-19 severity traits to either cell type programs (genes enriched in a cell type in each tissue) or disease progression programs (genes differentially expressed between COVID-19 and controls in a cell type) in each tissue using sc-linker<sup>47</sup> (Methods). AT2 (4.8x heritability enrichment, p-value=0.04), CD8 T (4.4x, p-value=0.009), and ciliated cell programs in the lung, proximal convoluted tubule and connecting tubule programs in kidney, and cholangiocyte programs in liver attained nominal (but not Bonferroni-corrected) significance (Extended Data Fig. 12g-h, Supplementary Information Table 11). Of all disease progression programs, only the club cell program (single-cell level model) had nominally significant heritability enrichment (10.5x, p-value=0.04 for severe COVID-19) (Extended Fig. 12g, Supplementary Information Table 11).

The highest number of driving genes was observed for lung AT2 cells and spanned several loci, hinting at a polygenic architecture linking AT2 cells with severe COVID-19 (Methods, Supplementary Information Table 11). Implicated GWAS proximity genes include *OAS3* in lung AT2 and club cells and *SLC4A7* in lung CD8 T cells (Supplementary Information Table 11), as well genes at unresolved significantly associated GWAS loci (Extended Data Fig. 12i), such as *FYCO1* (AT2, ciliated, club; chr3p), *NFKB1Z* (AT2; chr3q), and *DPP9* (AT2; chr 19) (Supplementary Information Table 11).

### Discussion

We built a biobank of severe COVID-19 autopsy tissue and atlases of COVID-19 lung, heart, liver, and kidney (Extended Data Fig. 12j), complementing a sister lung atlas (Melms *et al.*, companion manuscript).

Among the changes in lung cell composition in COVID-19, is a reduction in AT2 cells and the presence of PATS and IPBLP-like cells, suggesting that multiple regenerative strategies are invoked to re-establish alveolar epithelial cells lost to infection. A serial failure of epithelial progenitors

to regenerate at a sufficient rate, first by secretory progenitor cells in the nasal passages and large and small airways, followed by alveolar AT2 cells, PATS, and IPBLP cells, may eventually lead to lung failure.

Viral RNA in the lung varied significantly, was negatively correlated with S/s to death, and primarily detected in myeloid and endothelial cells (as in nonhuman primates<sup>48</sup>); spatial analysis supports high viral levels at the earlier stages of infection<sup>36,37,49</sup>. Epithelial cells were not enriched in high viral RNA samples or in SARS-CoV-2+ cells, consistent with their excessive death. Cell-associated SARS-CoV-2 UMIs may represent a mix of replicating virus, immune cell engulfment, and virions or virally-infected cells attached to the cell surface. We did not detect viral RNA in the heart, liver or kidney, but observed other changes, including broad upregulation of *PLCG2* in heart, a target of Bruton's tyrosine kinase (BTK)<sup>50</sup>.

Combining our profiles with GWAS of COVID-19, we related specific cell types to heritable risk, especially AT2, ciliated, and CD8<sup>+</sup> T cells and macrophages, as well as genes in multi gene regions underlying the association. This analysis can improve as GWAS grows and atlases expand.

Our study was limited by a modest number of donors without pre-selection of features, the terminal time point, limited distinction between viral RNA and true infection, and technical confounders such as PMI. Nevertheless, our methods would enable studies in diverse diseased or damaged tissues, future meta-analyses will further enhance its power, and provide critical resources for the community studying host-SARS-CoV-2 biology.

### Online content

Any methods, additional references, Nature Research reporting summaries, source data, extended data, supplementary information, acknowledgements, peer review information; details of author contributions and competing interests; and statements of data and code availability are available at <https://doi.org/10.1038/s41586-021-03570-8>.

1. Guan, W.-J. *et al.* Clinical Characteristics of Coronavirus Disease 2019 in China. *N. Engl. J. Med.* **382**, 1708–1720 (2020).
2. Puelles, V. G. *et al.* Multiorgan and Renal Tropism of SARS-CoV-2. *N. Engl. J. Med.* **383**, 590–592 (2020).
3. Huang, C. *et al.* Clinical features of patients infected with 2019 novel coronavirus in Wuhan, China. *Lancet* **395**, 497–506 (2020).
4. Xu, Z. *et al.* Pathological findings of COVID-19 associated with acute respiratory distress syndrome. *Lancet Respir Med* **8**, 420–422 (2020).
5. Varga, Z. *et al.* Endothelial cell infection and endotheliitis in COVID-19. *Lancet* **395**, 1417–1418 (2020).
6. Chen, G. *et al.* Clinical and immunological features of severe and moderate coronavirus disease 2019. *J. Clin. Invest.* **130**, 2620–2629 (2020).
7. Qin, C. *et al.* Dysregulation of Immune Response in Patients With Coronavirus 2019 (COVID-19) in Wuhan, China. *Clinical Infectious Diseases* **vol. 71** 762–768 (2020).
8. Hadjadj, J. *et al.* Impaired type I interferon activity and exacerbated inflammatory responses in severe Covid-19 patients. <https://doi.org/10.1101/2020.04.19.20068015>.
9. Bian, X.-W. *et al.* Autopsy of COVID-19 patients in China. *Natl Sci Rev* **7**, 1414–1418 (2020).
10. Menter, T. *et al.* Postmortem examination of COVID-19 patients reveals diffuse alveolar damage with severe capillary congestion and variegated findings in lungs and other organs suggesting vascular dysfunction. *Histopathology* **77**, 198–209 (2020).
11. Wichmann, D. *et al.* Autopsy Findings and Venous Thromboembolism in Patients With COVID-19: A Prospective Cohort Study. *Ann. Intern. Med.* **173**, 268–277 (2020).
12. Bösmüller, H. *et al.* The evolution of pulmonary pathology in fatal COVID-19 disease: an autopsy study with clinical correlation. *Virchows Arch.* **477**, 349–357 (2020).
13. Slyper, M. *et al.* A single-cell and single-nucleus RNA-Seq toolbox for fresh and frozen human tumors. *Nat. Med.* **26**, 1307 (2020).
14. Fleming, S. J., Marioni, J. C. & Babadi, M. CellBender remove-background: a deep generative model for unsupervised removal of background noise from scRNA-seq datasets. *bioRxiv* (2019).
15. Li, B. *et al.* Cumulus provides cloud-based data analysis for large-scale single-cell and single-nucleus RNA-seq. *Nat. Methods* **17**, 793–798 (2020).
16. Shaffer, A. L. *et al.* Blimp-1 orchestrates plasma cell differentiation by extinguishing the mature B cell gene expression program. *Immunity* **17**, 51–62 (2002).
17. Martins, G. & Calame, K. Regulation and functions of Blimp-1 in T and B lymphocytes. *Annu. Rev. Immunol.* **26**, 133–169 (2008).
18. Schupp, J. C. *et al.* Integrated Single Cell Atlas of Endothelial Cells of the Human Lung. *Cold Spring Harbor Laboratory* 2020.10.21.347914 (2020) <https://doi.org/10.1101/2020.10.21.347914>.
19. Travaglini, K. J. *et al.* A molecular cell atlas of the human lung from single-cell RNA sequencing. *Nature* (2020) <https://doi.org/10.1038/s41586-020-2922-4>.

20. Strunz, M. *et al.* Alveolar regeneration through a Krt8+ transitional stem cell state that persists in human lung fibrosis. *Nat. Commun.* **11**, 3559 (2020).
21. Kobayashi, Y. *et al.* Persistence of a regeneration-associated, transitional alveolar epithelial cell state in pulmonary fibrosis. *Nat. Cell Biol.* **22**, 934–946 (2020).
22. Choi, J. *et al.* Inflammatory Signals Induce AT2 Cell-Derived Damage-Associated Transient Progenitors that Mediate Alveolar Regeneration. *Cell Stem Cell* **27**, 366–382.e7 (2020).
23. Ziegler, C. G. K. *et al.* SARS-CoV-2 Receptor ACE2 Is an Interferon-Stimulated Gene in Human Airway Epithelial Cells and Is Detected in Specific Cell Subsets across Tissues. *Cell* **181**, 1016–1035.e19 (2020).
24. Sungnak, W. *et al.* SARS-CoV-2 entry factors are highly expressed in nasal epithelial cells together with innate immune genes. *Nat. Med.* **26**, 681–687 (2020).
25. Muus, C. *et al.* Single-cell meta-analysis of SARS-CoV-2 entry genes across tissues and demographics. *Nat. Med.* **27**, 546–559 (2021).
26. Xu, J. *et al.* SARS-CoV-2 induces transcriptional signatures in human lung epithelial cells that promote lung fibrosis. *Respir. Res.* **21**, 182 (2020).
27. Grillo, F., Barisione, E., Ball, L., Mastracci, L. & Fiocca, R. Lung fibrosis: an undervalued finding in COVID-19 pathological series. *Lancet Infect. Dis.* (2020) [https://doi.org/10.1016/S1473-3099\(20\)30582-X](https://doi.org/10.1016/S1473-3099(20)30582-X).
28. Vaughan, A. E. *et al.* Lineage-negative progenitors mobilize to regenerate lung epithelium after major injury. *Nature* **517**, 621–625 (2015).
29. Fernanda de Mello Costa, M., Weiner, A. I. & Vaughan, A. E. Basal-like Progenitor Cells: A Review of Dysplastic Alveolar Regeneration and Remodeling in Lung Repair. *Stem Cell Reports* **15**, 1015–1025 (2020).
30. Wölfel, R. *et al.* Virological assessment of hospitalized patients with COVID-2019. *Nature* **581**, 465–469 (2020).
31. Walsh, K. A. *et al.* SARS-CoV-2 detection, viral load and infectivity over the course of an infection. *J. Infect.* **81**, 357–371 (2020).
32. Blanco-Melo, D. *et al.* Imbalanced Host Response to SARS-CoV-2 Drives Development of COVID-19. *Cell* **181**, 1036–1045.e9 (2020).
33. Johnson, N. F. Release of lamellar bodies from alveolar type 2 cells. *Thorax* **35**, 192–197 (1980).
34. Grant, R. A. *et al.* Circuits between infected macrophages and T cells in SARS-CoV-2 pneumonia. *Nature* (2021) <https://doi.org/10.1038/s41586-020-03148-w>.
35. Butler, D. *et al.* Shotgun transcriptome, spatial omics, and isothermal profiling of SARS-CoV-2 infection reveals unique host responses, viral diversification, and drug interactions. *Nat. Commun.* **12**, 1660 (2021).
36. Park, J. *et al.* Systemic Tissue and Cellular Disruption from SARS-CoV-2 Infection revealed in COVID-19 Autopsies and Spatial Omics Tissue Maps. *Cold Spring Harbor Laboratory* 2021.03.08.434433 (2021) <https://doi.org/10.1101/2021.03.08.434433>.
37. Rendeiro, A. F. *et al.* The spatio-temporal landscape of lung pathology in SARS-CoV-2 infection. *medRxiv* (2020) <https://doi.org/10.1101/2020.10.26.20219584>.
38. Karki, R. *et al.* Synergism of TNF- $\alpha$  and IFN- $\gamma$  Triggers Inflammatory Cell Death, Tissue Damage, and Mortality in SARS-CoV-2 Infection and Cytokine Shock Syndromes. *Cell* **184**, 149–168.e17 (2021).
39. Subramanian, A. *et al.* Gene set enrichment analysis: a knowledge-based approach for interpreting genome-wide expression profiles. *Proc. Natl. Acad. Sci. U. S. A.* **102**, 15545–15550 (2005).
40. Mootha, V. K. *et al.* PGC-1 $\alpha$ -responsive genes involved in oxidative phosphorylation are coordinately downregulated in human diabetes. *Nat. Genet.* **34**, 267–273 (2003).
41. van de Sandt, C. E. *et al.* Human CD8+ T Cells Damage Noninfected Epithelial Cells during Influenza Virus Infection In Vitro. *Am. J. Respir. Cell Mol. Biol.* **57**, 536–546 (2017).
42. Short, K. R. *et al.* Influenza virus damages the alveolar barrier by disrupting epithelial cell tight junctions. *Eur. Respir. J.* **47**, 954–966 (2016).
43. Lemieux, J. E. *et al.* Phylogenetic analysis of SARS-CoV-2 in Boston highlights the impact of superspreading events. *Science* **371**, (2021).
44. Yu, H. H. & Zallen, J. A. Abl and Cncaof/Afadin mediate mechanotransduction at tricellular junctions. *Science* **370**, (2020).
45. COVID-19 Host Genetics Initiative. The COVID-19 Host Genetics Initiative, a global initiative to elucidate the role of host genetic factors in susceptibility and severity of the SARS-CoV-2 virus pandemic. *Eur. J. Hum. Genet.* **28**, 715–718 (2020).
46. Severe Covid-19 GWAS Group *et al.* Genomewide Association Study of Severe Covid-19 with Respiratory Failure. *N. Engl. J. Med.* **383**, 1522–1534 (2020).
47. Jagadeesh, K. A. *et al.* Identifying disease-critical cell types and cellular processes across the human body by integration of single-cell profiles and human genetics. *Cold Spring Harbor Laboratory* 2021.03.19.436212 (2021) <https://doi.org/10.1101/2021.03.19.436212>.
48. Speranza, E. *et al.* SARS-CoV-2 infection dynamics in lungs of African green monkeys. *Cold Spring Harbor Laboratory* 2020.08.20.258087 (2020) <https://doi.org/10.1101/2020.08.20.258087>.
49. Desai, N. *et al.* Temporal and Spatial Heterogeneity of Host Response to SARS-CoV-2 Pulmonary Infection. *medRxiv* (2020) <https://doi.org/10.1101/2020.07.30.20165241>.
50. Liu, T.-M. *et al.* Hypermorph mutation of phospholipase C,  $\gamma 2$  acquired in ibritinib-resistant CLL confers BTK independency upon B-cell receptor activation. *Blood* **126**, 61–68 (2015).

**Publisher's note** Springer Nature remains neutral with regard to jurisdictional claims in published maps and institutional affiliations.

© The Author(s), under exclusive licence to Springer Nature Limited 2021

<sup>1</sup>Klarman Cell Observatory, Broad Institute of MIT and Harvard, Cambridge, MA, 02142, USA.

<sup>2</sup>Broad Institute of MIT and Harvard, Cambridge, MA, 02142, USA. <sup>3</sup>Program in Health Sciences & Technology, Harvard Medical School & Massachusetts Institute of Technology, Boston, MA, 02115, USA. <sup>4</sup>Institute for Medical Engineering & Science, Massachusetts Institute

of Technology, Cambridge, MA, 02139, USA. <sup>5</sup>Koch Institute for Integrative Cancer Research, Massachusetts Institute of Technology, Cambridge, MA, 02139, USA. <sup>6</sup>Ragon Institute of MGH, MIT, and Harvard, Cambridge, MA, 02139, USA. <sup>7</sup>Harvard Graduate Program in Biophysics, Harvard University, Cambridge, MA, 02138, USA. <sup>8</sup>Center for Immunology and Inflammatory Diseases, Department of Medicine, Massachusetts General Hospital, Boston, MA, 02114, USA. <sup>9</sup>Center for Cancer Research, Massachusetts General Hospital, Harvard Medical School, Boston, MA, 02114, USA. <sup>10</sup>Harvard Medical School, Boston, MA, 02115, USA. <sup>11</sup>Massachusetts Institute of Technology, Cambridge, MA, 02139, USA. <sup>12</sup>Data Sciences Platform, Broad Institute of MIT and Harvard, Cambridge, MA, 02142, USA. <sup>13</sup>Precision Cardiology Laboratory, Broad Institute of MIT and Harvard, Cambridge, MA, 02142, USA. <sup>14</sup>Department of Epidemiology, Harvard School of Public Health, Boston, USA. <sup>15</sup>Division of Infectious Diseases, Department of Medicine, Massachusetts General Hospital, Boston, MA, 02114, USA. <sup>16</sup>Department of Medicine, Harvard Medical School, Boston, MA, 02115, USA. <sup>17</sup>Department of Pathology, Beth Israel Deaconess Medical Center, Boston, MA, 02115, USA. <sup>18</sup>Harvard Medical School Initiative for RNA Medicine, Boston, MA, 02115, USA. <sup>19</sup>Cancer Research Institute, Beth Israel Deaconess Medical Center, Boston, MA, 02115, USA. <sup>20</sup>Department of Medicine, Division of Hematology/Oncology, Columbia University Irving Medical Center, New York, NY, USA. <sup>21</sup>Columbia Center for Translational Immunology, New York, NY, USA. <sup>22</sup>Infectious Disease and Microbiome Program, Broad Institute of MIT and Harvard, Cambridge, MA, 02142, USA. <sup>23</sup>Institute for Molecular Medicine Finland, Helsinki, Finland. <sup>24</sup>Analytical & Translational Genetics Unit, Massachusetts General Hospital, Harvard Medical School, Boston, MA, 02115, USA. <sup>25</sup>Department of Pathology and Cell Biology, Columbia University Irving Medical Center, New York, NY, USA. <sup>26</sup>Department of Medicine, Beth Israel Deaconess Medical Center, Boston, MA, 02115, USA. <sup>27</sup>Division of Gastroenterology, Hepatology and Nutrition, Department of Medicine, Beth Israel Deaconess Medical Center, Boston, MA, 02115, USA. <sup>28</sup>Department of Systems Biology, Harvard Medical School, Boston, MA, 02115, USA. <sup>29</sup>FAS Center for Systems Biology, Department of Organismic and Evolutionary Biology, Harvard University, Cambridge, MA, 02138, USA. <sup>30</sup>Division of Endocrinology, Diabetes, and Metabolism, Beth Israel Deaconess Medical Center, Boston, MA, 02115, USA. <sup>31</sup>Boston Nutrition and Obesity Research Center Functional Genomics and Bioinformatics Core Boston, Boston, MA, 02115, USA. <sup>32</sup>Department of Organismic and Evolutionary Biology, Harvard University, Cambridge, MA, USA. <sup>33</sup>Divisions of Cardiovascular Medicine and Genetics, Brigham and Women's Hospital, Harvard Medical School, Boston, MA, 02115, USA. <sup>34</sup>NanoString Technologies Inc., Seattle, WA, 98109, USA. <sup>35</sup>Department of Radiology, Beth Israel Deaconess Medical Center, Boston, MA, 02215, USA. <sup>36</sup>Department of Pathology, Massachusetts General Hospital, Harvard Medical School, Boston, MA, 02115, USA. <sup>37</sup>Department of Genetics and BASE Initiative, Stanford University School of Medicine, Stanford, USA. <sup>38</sup>Massachusetts General Hospital Cancer Center, Department of Medicine, Massachusetts General Hospital, Boston, MA, 02114, USA. <sup>39</sup>Center for Genetic Epidemiology, Department of Preventive Medicine, Keck School of Medicine, University of Southern California, Los Angeles, CA, USA. <sup>40</sup>Department of Pathology, Brigham and Women's Hospital, Boston, MA, 02115, USA. <sup>41</sup>John A. Paulson School of Engineering and Applied Sciences, Harvard University, Cambridge, MA, 02138, USA. <sup>42</sup>Harvard-MIT Division of Health Sciences and Technology, Cambridge, MA, USA. <sup>43</sup>Department of Pathology, Harvard Medical School, Boston, MA, 02115, USA. <sup>44</sup>Harvard Stem Cell Institute, Cambridge, MA, USA. <sup>45</sup>Center for Regenerative Medicine, Massachusetts General Hospital, Boston, MA, 02114, USA. <sup>46</sup>Infectious Diseases Division, Department of Medicine, Brigham and Women's Hospital, Boston, MA, USA. <sup>47</sup>Department of Medicine, Massachusetts General Hospital, Harvard Medical School, Boston, MA, 02114, USA. <sup>48</sup>Department of Cell Biology, Duke University School of Medicine, Durham, NC, USA. <sup>49</sup>Cardiovascular Disease Initiative, The Broad Institute of MIT and Harvard, Cambridge, MA, USA. <sup>50</sup>Department of Genetics, Harvard Medical School, Boston, MA, 02115, USA. <sup>51</sup>Department of Molecular Biology and Center for Computational and Integrative Biology, Massachusetts General Hospital, Boston, MA, 02114, USA. <sup>52</sup>Department of Immunology and Infectious Diseases, Harvard T.H. Chan School of Public Health, Harvard University, Boston, MA, USA. <sup>53</sup>Howard Hughes Medical Institute, Chevy Chase, MD, USA. <sup>54</sup>Massachusetts Consortium on Pathogen Readiness, Boston, MA, USA. <sup>55</sup>Wyss Institute for Biologically Inspired Engineering, Harvard University, Boston, USA. <sup>56</sup>Massachusetts General Hospital, Boston, MA, 02114, USA. <sup>57</sup>Vascular Biology Program and Department of Surgery, Boston Children's Hospital, Harvard Medical School, Boston, MA, USA. <sup>58</sup>Herbert Irving Comprehensive Cancer Center, Columbia University Irving Medical Center, New York, NY, USA. <sup>59</sup>Program for Mathematical Genomics, Columbia University Irving Medical Center, New York, NY, USA. <sup>60</sup>Program in Computational & Systems Biology, Massachusetts Institute of Technology, Cambridge, MA, 02139, USA. <sup>61</sup>Program in Immunology, Harvard Medical School, Boston, MA, 02115, USA. <sup>62</sup>Department of Chemistry, Massachusetts Institute of Technology, Cambridge, MA, 02139, USA. <sup>63</sup>Present address: Genentech, 1 DNA Way, South San Francisco, CA, USA. <sup>64</sup>These authors contributed equally: Toni M. Delorey, Carly G. K. Ziegler, Graham Heimberg, Rachelly Normand, Yiming Yang, Åsa Segerstolpe, Domenic Abbondanza, Stephen J. Fleming, Ayshwarya Subramanian, Daniel T. Montoro, Karthik A. Jagadeesh, Kushal K. Dey, Pritha Sen, Michal Slyper, Yered H. Pita-Juárez, Devan Phillips, Jana Biermann. <sup>65</sup>These authors jointly supervised this work: Patrick T. Ellinor, Deborah Hurig, Pardis C. Sabeti, Richard Novak, Robert Rogers, Donald E. Ingber, Z. Gordon Jiang, Dejan Jung, Mehrtaq Babadi, Samouil L. Farhi, Benjamin Izar, James R. Stone, Ioannis S. Vlachos, Isaac H. Solomon, Orr Ashenberg, Caroline B. M. Porter, Bo Li, Alex K. Shalek, Alexandra-Chloé Villani, Orit Rozenblatt-Rosen, Aviv Regev. <sup>✉</sup>e-mail: [ivlachos@bidmc.harvard.edu](mailto:ivlachos@bidmc.harvard.edu); [shalek@mit.edu](mailto:shalek@mit.edu); [avillani@mgh.harvard.edu](mailto:avillani@mgh.harvard.edu); [orit.r.rosen@gmail.com](mailto:orit.r.rosen@gmail.com); [aviv.regev.sc@gmail.com](mailto:aviv.regev.sc@gmail.com)

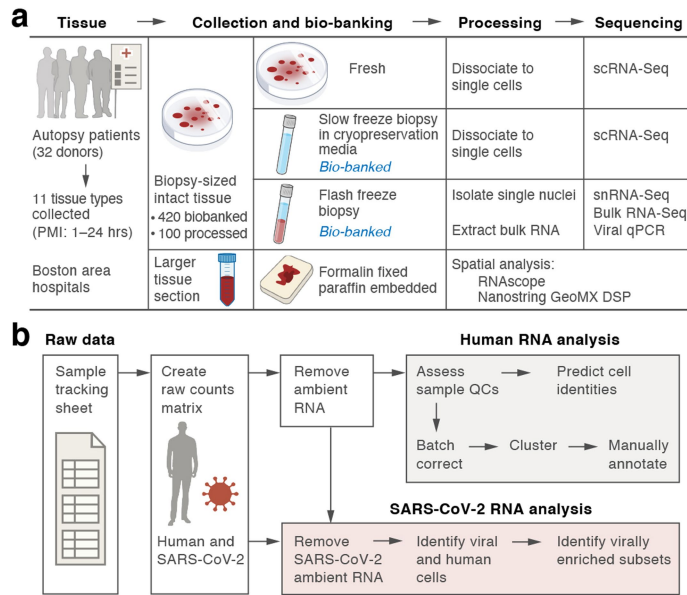


**Fig. 1 | Experimental and computational pipeline for a COVID-19 autopsy atlas. a.** Sample processing pipeline. Up to 11 tissue types from 32 donors were collected. PMI: post-mortem interval. **b.** sc/snRNA-Seq analysis pipeline.

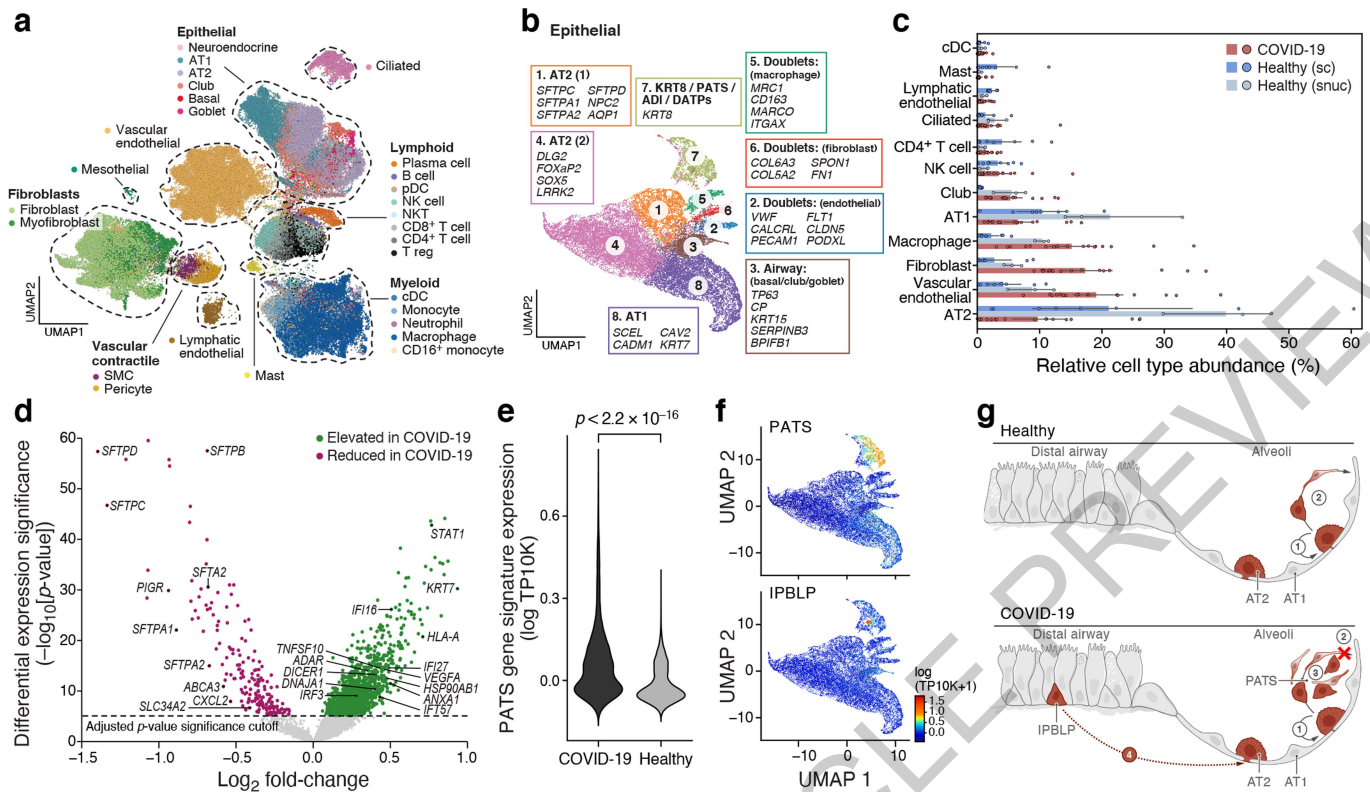


**Fig. 2 | A single cell and single nucleus atlas of COVID-19 lung. a.** Automatic prediction identifies 28 cell subsets across compartments. UMAP embedding of 106,792 harmonized sc/snRNA-Seq profiles (dots) from 24 tissue samples of 16 COVID-19 lung donors, colored by automatic annotations (legend). **b.** Epithelial cell subsets. UMAP embedding of 21,661 epithelial cells/nuclei profiles, colored by manual annotations, with highly expressed marker genes (boxes). **c, d.** Cell composition and expression differences between COVID-19 and healthy lung. **c.** Cell proportions (x axis, mean: bar, and 95% confidence intervals: line) in each automatically annotated subset (y axis) in COVID-19 snRNA-Seq (red, n=16), healthy snRNA-Seq (grey, n=3), and healthy scRNA-seq (n=8, blue). Cell types shown have a COVID-19 *vs.* healthy snRNA-Seq FDR < 0.05 (Dirichlet-multinomial regression). **d.** Significance (-Log<sub>10</sub>(P-value), y axis) *vs.* magnitude (log<sub>2</sub>(fold-change), x axis) of differential expression of each gene

(dots; horizontal dashed line: FDR < 0.05) between COVID-19 and healthy lung from a total of 2,000 AT2 cells and 14 studies (2 sided test, Methods). **e, f.** An increased PATS<sup>20-22</sup> program in pneumocytes in COVID-19 *vs.* healthy lung. **e.** Distribution of PATS signature scores (y axis) for 17,655 cells from COVID-19 and 24,000 cells from healthy lung pneumocytes (x axis) p-value <  $2.2 \times 10^{-16}$  (one-sided Mann-Whitney U test). **f.** UMAP embedding of 21,661 epithelial cell profiles (dots) colored by signature level (color legend, lower right) for the PATS (top) or IPBLP (bottom) programs. **g.** Model of epithelial cell regeneration in healthy and COVID-19 lung. In healthy alveoli (top), AT2 cells self-renew (1) and differentiate into AT1 cells (2). In COVID-19 alveoli (bottom), AT2 cell self-renewal (1) and AT1 differentiation (2) are inhibited, resulting in PATS accumulation (3) and recruitment of airway-derived IPBLP progenitors to alveoli (4).



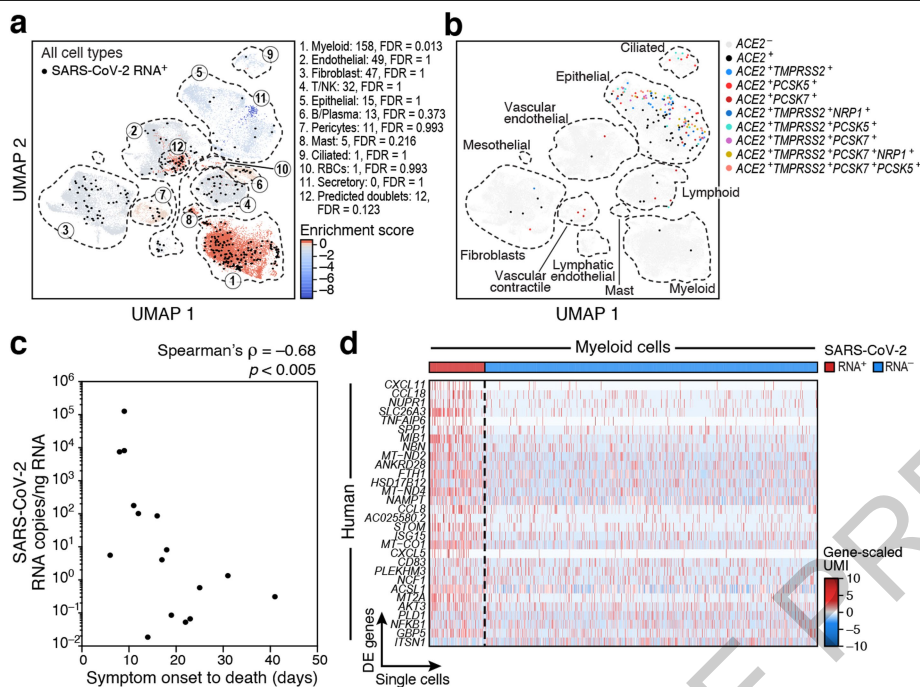


**Fig. 3 | SARS-CoV-2 RNA<sup>+</sup> single cells are enriched for phagocytic and endothelial cells. a, b.** Many SARS-CoV-2 RNA<sup>+</sup> single cells do not express known SARS-CoV-2 entry factors. UMAP embedding of all 106,792 lung cells/nuclei (as in Fig. 2a), showing either **a.** only the 40,581 cells from seven donors containing any SARS-CoV-2 RNA<sup>+</sup> cell, colored by viral enrichment score (Methods, red: stronger enrichment) and by SARS-CoV-2 RNA<sup>+</sup> cells (black points), and marked by annotation and FDR of enrichment (legend) or **b.** all 106,792 cells/nuclei, colored by expression of SARS-CoV-2 entry factors (co-expression combinations with at least 10 cells are shown). Dashed lines:

major cell types. **c.** Reduction in SARS-CoV-2 RNA with prolonged S/s to death interval (Spearman  $\rho = -0.68$ ,  $p < 0.005$ , two-sided test). S/s to death ( $x$  axis, days) and lung SARS-CoV-2 copies/ng input RNA ( $y$  axis) for each donor ( $n=16$ ). **d.** Expression changes in SARS-CoV-2 RNA<sup>+</sup> myeloid cells. Significantly differentially expressed host genes (log-normalized and scaled digital gene expression, rows; cutoff: FDR < 0.05 and  $\log_2$  fold change > 0.5) across SARS-CoV-2 RNA<sup>+</sup> ( $n=158$ ) and SARS-CoV-2 RNA<sup>-</sup> myeloid cells ( $n=790$ ) (columns).

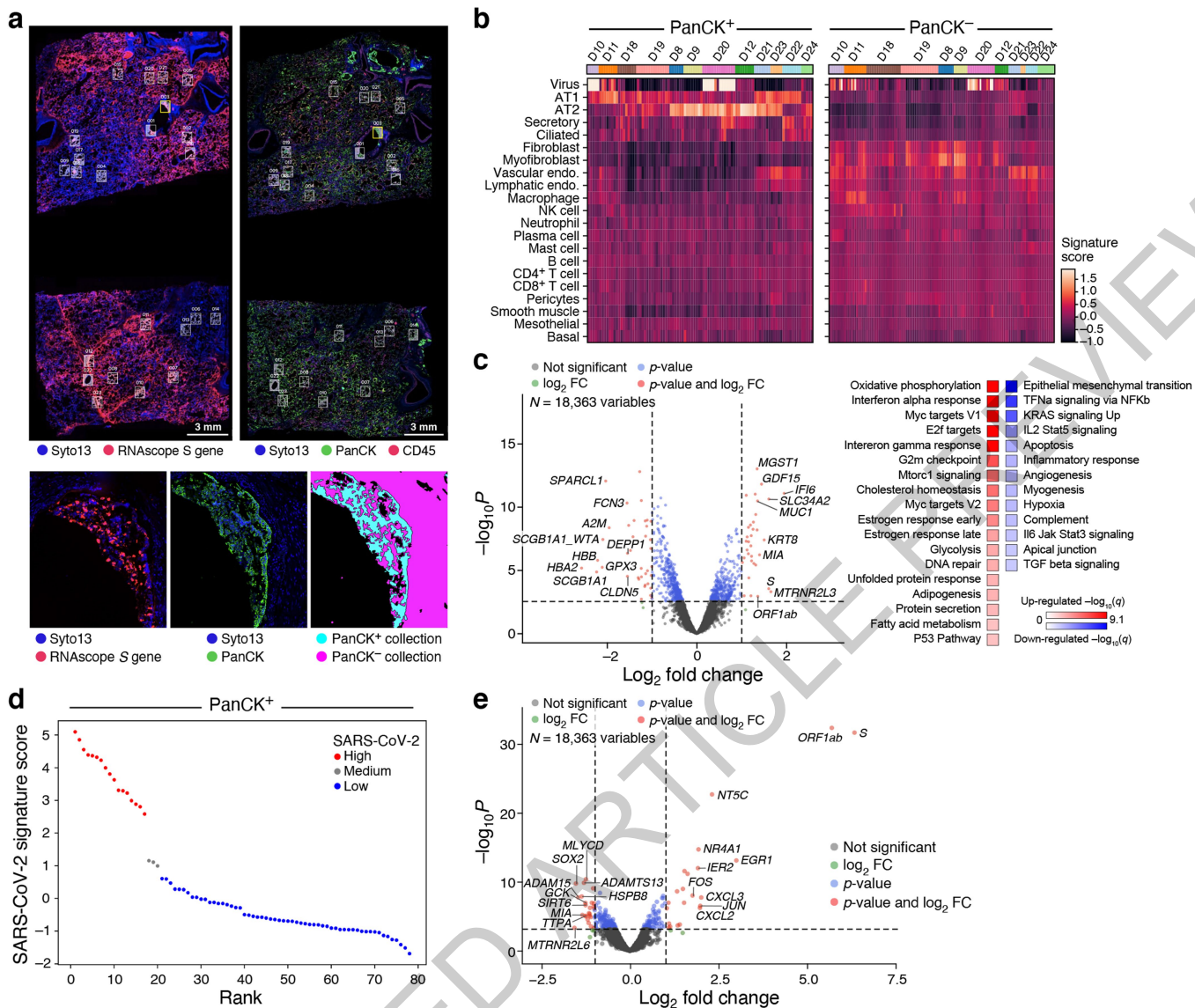


**Fig. 4 | Composition and expression differences between COVID-19 and healthy lungs and between infected and uninfected regions within COVID-19 lungs.** **a.** Example of analyzed regions. Top: RNAscope (left) and immunofluorescent staining (right) of donor D20 with collection ROIs and matched areas in white rectangles. Bottom: One ROI (yellow rectangle) from each scan (left and middle), and the segmented collection AOs (right). **b.** Cell composition differences between PanCK<sup>+</sup> and PanCK<sup>-</sup> alveolar AOs and between AOs from COVID-19 ( $n=9,190$  AOs) and healthy (D22-24, 38 AOs) lungs. Expression scores (color bar) of cell type signatures (rows) in PanCK<sup>+</sup> (left) and PanCK<sup>-</sup> (right) alveolar AOs (columns) in WTA data from different donors (top color bar). **c.** Differential gene expression in COVID-19 *vs.* healthy lung. Left: Significance ( $-\log_{10}(p\text{-value})$ , y axis) and magnitude ( $\log_2(\text{fold-change})$ , x axis) of differential expression of each gene (dots) in WTA

data between PanCK<sup>+</sup> alveoli AOs from COVID-19 ( $n=78$ ) *vs.* healthy ( $n=18$ ) lung. Right: Significance ( $-\log_{10}(q\text{-value})$ ) of enrichment (permutation test) of different pathways (rows). **d, e.** Changes in gene expression in SARS-CoV-2 high *vs.* low AOs within COVID-19 lungs in WTA data. **d.** SARS-CoV-2 high and low alveolar AOs. PanCK<sup>+</sup> alveolar AOs (dots) rank ordered by their SARS-CoV-2 signature scores (y axis) in WTA data, and partitioned to high (red), medium (grey) and low (blue) SARS-CoV-2 AOs. **e.** Significance ( $-\log_{10}(p\text{-value})$ , y axis) and magnitude ( $\log_2(\text{fold-change})$ , x axis) of differential expression of each gene (dots) in WTA data between SARS-CoV-2 high and low AOs for PanCK<sup>+</sup> alveoli (AOs: 17 high, 3 medium, 58 low). Horizontal dashed line: FDR = 0.05. Vertical dashed lines:  $|\log_2(\text{fold-change})| = 2$ . Top 10 DE genes by fold change marked.

# Article

## Reporting summary

Further information on research design is available in the Nature Research Reporting Summary linked to this paper.

## Code availability

All samples were initially processed using Cumulus (<https://github.com/klarman-cell-observatory/cumulus>), which we ran on the Terra Cloud platform (<https://app.terra.bio/>). Code for all other analyses is available on GitHub (<https://github.com/klarman-cell-observatory/covid19-autopsy>).

## Data availability

Processed sequencing data (sc/snRNA-Seq and bulk) are available in the Gene Expression Omnibus (GEO, <https://www.ncbi.nlm.nih.gov/geo/>) under accession no. GSE171668 and raw human sequencing data is available in the controlled access repository DUOS (<https://duos.broadinstitute.org/>), under Dataset IDs DUOS-000126, DUOS-000127, DUOS-000128 and DUOS-000129. Viral genome assemblies and short-read sequencing data are publicly available on NCBI's Genbank and SRA databases, respectively, under BioProject PRJNA720544. GenBank accessions for SARS-CoV-2 genomes are MW885875-MW885883. Data for other tissues in the biobank will be released as they are acquired. The processed data is available on the Single Cell Portal: Lung - [https://singlecell.broadinstitute.org/single\\_cell/study/SCP1052/](https://singlecell.broadinstitute.org/single_cell/study/SCP1052/) Heart - [https://singlecell.broadinstitute.org/single\\_cell/study/SCP1216/](https://singlecell.broadinstitute.org/single_cell/study/SCP1216/) Kidney - [https://singlecell.broadinstitute.org/single\\_cell/study/SCP1214/](https://singlecell.broadinstitute.org/single_cell/study/SCP1214/) Liver - [https://singlecell.broadinstitute.org/single\\_cell/study/SCP1213/](https://singlecell.broadinstitute.org/single_cell/study/SCP1213/) Nanostring GeoMx raw and normalized count matrices are available on GEO under accession no. GSE163530. Raw images will be available upon request. Source data are provided with this paper.

**Acknowledgements** We are deeply grateful to all donors and their families. This paper is part of the Human Cell Atlas (<https://www.humancellatlas.org/publications/>). We acknowledge the contribution of Casey Kania, Emmaline Kounaves, Nichole Lemelin, Justin Susterich, Jessica Teixeira, Claudia Bernal, Max Berstein, Allison Morris, Jordan N. Ray, Amanda Awley, Amanda Araujo and Erika Figueroa who all assisted in performing the autopsies at the Massachusetts General Hospital. We thank Ania Hupalowska and Leslie Gaffney for help with figure preparation. We thank Molly Veregge, Zachary Kramer, and Christopher Jacobs for their contributions in the execution of experimental procedures, and Dimitra Pouli who supported the creation of tissue annotation resources. We thank 10x Genomics, Illumina, BD Biosciences, and NanoString for help and support with instruments and/or lab reagents and technical advice. Portions of this research were conducted on the Ithaca High Performance Computing system, Department of Pathology, BIDMC, and the O2 High Performance Compute Cluster at Harvard Medical School. This project has been funded in part with funds from the Manton Foundation, Klarman Family Foundation, HHMI, the Chan Zuckerberg Initiative, and the Human Tumor Atlas Network trans-network projects SARDANA (Shared Repositories, Data, Analysis and Access). A.R. was an Investigator of the Howard Hughes Medical Institute. This project was also funded by DARPA grant HRO011-20-2-0040 (to D.E.I.) and the US Food and Drug Administration grant HHSF223201810172C (to P.C.S. and A.K.S.). A.-C.V. acknowledges funding support from the National Institute of Health Director's New Innovator Award (DP2CA247831), the Massachusetts General Hospital (MGH) Transformative Scholar in Medicine Award, a COVID-19 Clinical Trials Pilot grant from the Executive Committee on Research at MGH, and the Damon Runyon-Rachleff Innovation Award. G.S. acknowledges support from the NIH R01AA0207440 and U01AA026933 research grants. A.P. acknowledges funding from the

following sources U01HG009379, R01MH101244, R37MH107649. We thank all members of the Department of Pathology and Cell Biology at Columbia University Irving Medical Center who led the procurement of autopsy tissues used in this work. This work was supported by National Institute of Health (NIH) grants K08CA222663 (B.I.), R37CA258829 (B.I.), U54CA225088 (B.I.), FastGrants (B.I.), and the Burroughs Wellcome Fund Career Award for Medical Scientists (B.I.). This research was funded in part through the NIH/NCI Cancer Center Support Grant P30CA013696 at Columbia University and utilized the Molecular Pathology Shared Resource and its Tissue Bank.

**Author contributions** A.K.S., A.C.V., I.S.V., Z.G.J., O.R.-R., and A.R. conceived and led the study. These authors contributed equally as co-second authors: Z.B.-A., N.B., A.G., J.G., J.C.M., I.K., E.N., P.N., Y.V.P., S.S.R., S.N., L.T.-Y.T., K.J.S., M.Su., V.M.T., S.K.V., Y.W. T.M.D., C.G.K.Z., Å. S. D.A. designed protocols and carried out experiments together with D.P., Z.B.-A., V.M.T., A.S. S.Z., J.G., J.H., E.N., M.Su., C.M., L.T., A.E., D.Pa., L.P., J.C.M., L.A.-Z. C.B.M.P., C.G.K.Z., O.A., R.N., G.H., K.J., K.S., B.L., Y.Y., S.F., A.S., P.N., Y.P.J., P.N., T.He., J.R., W.H., I.S.V., T.M.D. and J.B. designed and performed computational analysis. M.B., N.B., J.G., Y.W., R.G., S.S.R., H.M., P.S., A.W., C.M., M. L.-G., T.H., D.T.M., S.W., D.R.Z., E.R., M.R. E.M., R.F., P.Di., A.G., C.Pe. and M.N. provided input to and assisted with computational analysis. K.J., K.D., A.G., J.E., S.G., A.R. and A.P., contributed methods and performed integrated analysis for GWAS. P.R.T., D.T.M., Z.G.J., Y.P., G.S., S.N., S.R., and J.R. provided clinical and biological expertise. D.F., D.J., D.E.M., C.P., S.K.V., E.K. and J.S. provided clinical expertise, performed sample acquisition and/or administrative coordination at MGH. J.H., R.R. R.N., O.R.B., Z.G.J., Y.P., and D.I. provided clinical expertise, performed sample acquisition and/or administrative coordination at BIDMC. I.H.S., D.A., L.C., J.G., R.P., M.Si., provided clinical expertise, performed sample acquisition and/or administrative coordination at BWH. I.G., H.H., B.I. provided clinical expertise, performed sample acquisition and/or administrative coordination at CUIMC/NYP. P.D., D.P., J.J.-V., and J.B. helped with sample coordination and sample receipt at the Broad Institute. N.B. and S.R. performed bulk RNA-Seq deconvolution analysis. E.N., M.R. and K.S. performed viral qPCR, whole genome sequencing and phylogenetic analyses. M.S. provided input for sc/snRNA-Seq experiments and protocols. J.J.-V., E.T., O.R.R., and A.C.V. managed the study and tissue acquisition. T.L.T. contributed computational expertise and advice. T.M.D., C.B.M.P., C.G.K.Z., G.H., R.N., K.J., O.A., B.L., Z.G.J., I.S.V., Y.Y., S.F., A.S., D.T.M., A.K.S., A.C.V., O.R.-R. and A. Regev wrote the manuscript, with input from all authors. D.H., P.C.S., N.H., P.T.E. supervised research.

**Competing interests** A.R. is a co-founder and equity holder of Celsius Therapeutics, an equity holder in Immunitas, and was an SAB member of ThermoFisher Scientific, Syros Pharmaceuticals, Neogene Therapeutics and Asimov until July 31, 2020. From August 1, 2020, A.R. is an employee of Genentech. O.R.-R. is an employee of Genentech as of October 19, 2020. P.Di., R.F., E.M.M., M.Ro., E.H.R., L.P., T.He., J.R., J.B., and S.W. are employees and stockholders at Nanostring Technologies Inc. D.R.Z. is a former employee and stockholder at NanoString Technologies. N.H., holds equity in BioNTech and Related Sciences. T.H. is an employee and stockholder of Prime Medicine as of Oct. 13, 2020. G.H. is an employee of Genentech as of Nov 16, 2020. R.N. is a founder, shareholder, and member of the board at Rhinostics Inc. P.C.S. is a co-founder and shareholder of Sherlock Biosciences, and a Board member and shareholder of DanaHER Corporation. A.K.S. reports compensation for consulting and/or SAB membership from Honeycomb Biotechnologies, Cellarity, Repertoire Immune Medicines, Ochre Bio, and Dahlia Biosciences. Z.G.J. reports grant support from Gilead Science, Pfizer, compensation for consulting from Olix Pharmaceuticals. Y.V.P. reports grant support from Enanta Pharmaceuticals, CymaBay Therapeutics, Morphic Therapeutic; consulting and/or SAB in Ambys Medicines, Morphic Therapeutics, Enveda Therapeutics, BridgeBio Pharma, as well as being an Editor – American Journal of Physiology-Gastrointestinal and Liver Physiology. G.S. reports consultant service in Alnylam Pharmaceuticals, Merck, Generon, Glympse Bio, Inc., Mayday Foundation, Novartis Pharmaceuticals, Quest Diagnostics, Surrozen, Terra Firma, Zomagen Bioscience, Pandion Therapeutics, Inc. Durect Corporation; royalty from UpToDate Inc., and Editor service in Hepatology Communications. P.R.T. receives consulting fees from Cellarity Inc., and Surrozen Inc., for work not related to this manuscript. P.T.E. is supported by a grant from Bayer AG to the Broad Institute focused on the genetics and therapeutics of cardiovascular diseases. P.T.E. has also served on advisory boards or consulted for Bayer AG, Quest Diagnostics, MyoKardia and Novartis. B.I. is a consultant for Merck and Volastra Therapeutics. All other authors declare no competing interests.

## Additional information

**Supplementary information** The online version contains supplementary material available at <https://doi.org/10.1038/s41586-021-03570-8>.

**Correspondence and requests for materials** should be addressed to A.R., A.F.S., A.-C.V., I.S.V. or O.R.R.

**Peer review information** Nature thanks Christopher Mason, Michael Matthey and the other, anonymous, reviewer(s) for their contribution to the peer review of this work.

**Reprints and permissions information** is available at <http://www.nature.com/reprints>.

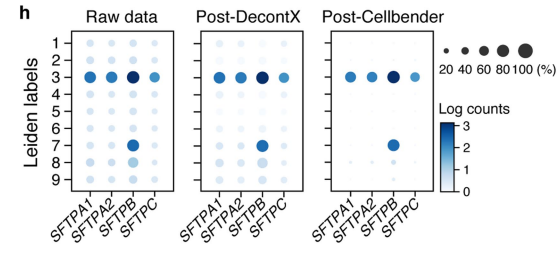
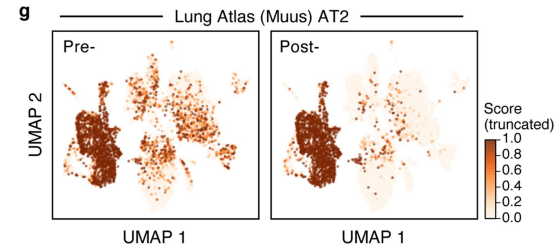
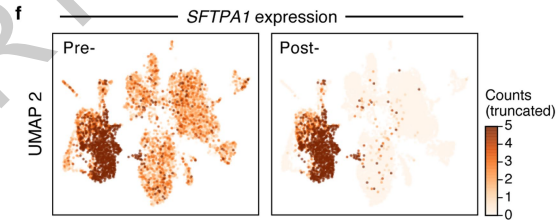
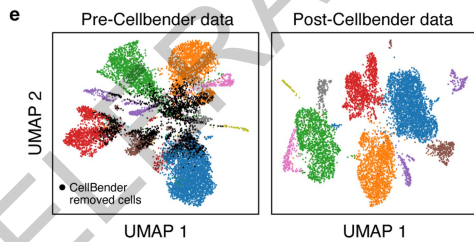
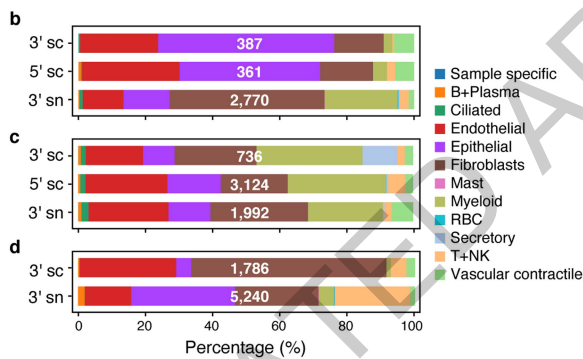
**a**

Patient					Lung	Heart	Liver	Kidney	Spleen	Trachea	Lymph node	Muscle	Nasal scraping	Oral scraping	Brain	Organ failure	IMV (days)	S/s to death (days)	PMI (h, min)
No	Race	Ethnicity	Sex	Age															
<b>Hospital site A</b>																			
D1	Other	Hispanic/ Latino	F	60-65	● n	● n	● n									Multi-organ	12	18	18 h
D2	Other	Hispanic/ Latino	M	65-70	● n	● n	● n									Multi-organ	7	12	20 h
D3	Black/ AA	—	M	30-35	● n c	● n	● n									Lung, heart	6	6	16 h
D4	Other	Hispanic/ Latino	M	40-45	● n	● n	● n	● n								Lung, kidney	9	22	15 h
D5	Black/ AA	—	F	> 89	● n	● n	● n	● n								Lung	0	19	10 h
D6	White	Not Hispanic/ Latino	M	65-70	● n	● n	● n	● n							●	Lung, neuro comp.	0	14	14 h
D7	White	Not Hispanic/ Latino	M	80-85	● n	● n	● n	● n								Lung	0	9	17 h
<b>Hospital site B</b>																			
D8	Black/ AA	Hispanic/ Latino	M	65-70	● s n c	● n	●	● n	●	●	●					Lung, kidney	15	23	21 h
D9	Black/ AA	Not Hispanic/ Latino	F	50-55	● s	●	●	●	●	●	●					Lung	0	7	21 h
D10	White	Not Hispanic/ Latino	M	50-55	● s n	● n	● n	● n	●	●	●		●			Multi-organ	4	8	20 h
D11	White	—	M	75-80	● s n	● n	● n	● n	●	●	●		●			Lung, kidney	4	7	24 h
D12	White	Not Hispanic/ Latino	M	40-45	● s n c	●	● n	● n	●	●	●		●	●		Multi-organ	22	22	24 h
D18	Black/ AA	—	F	65-70	● s	●	●	●	●	●	●					Lung	4	15	52 h
D19	Other	Hispanic/ Latino	M	55-60	● s	●	●	●	●	●	●					Lung	1	6	32 h
D20	White	—	F	65-70	● s	● s	●	●	●	● s	●					Lung, heart	1	1	12 h
D21	—	Hispanic/ Latino	M	55-60	● s	●	●	●	●	●	●					Lung	0	2	32 h
<b>Hospital site C</b>																			
D13	Black/ AA	Not Hispanic	M	> 89	● s n	● n	● n	●	●	●	●					Lung	0	11	1 h
D14	Black/ AA	Not Hispanic	F	80-85	● s n	● n	● n	● n	●	●	●					Lung	0	17	3 h 4 min
D15	—	—	F	55-60	● s n	● n	● n	● n	●	●	●					Lung, kidney	30	41	2 h 43 min
D16	Black/ AA	Not Hispanic	F	75-80	● s n	● n	● n	●	●	●	●					Lung, heart	13	16	1 h 30 min
D17	White	Not Hispanic	M	75-80	● s n	● n	● n	● n	●	●	●					Lung, heart, kidney	24	31	1 h 25 min
<b>Hospital site D</b>																			
D25	—	—	M	80-85				● n								Lung, heart	10	—	3 h
D26	—	Hispanic/ Latino	F	80-85				● n								Lung	25	27	4 h
D27	White	Not Hispanic/ Latino	M	70-75		● n										Heart	0	16	4 h
D28	—	—	F	> 89		● n										Lung, heart	0	11	2 h 30 min
D29	—	Hispanic/ Latino	F	75-80				● n								Lung	12	28	5 h
D30	—	Hispanic/ Latino	M	80-85				● n								Lung, kidney	—	28	4 h
D31	—	Hispanic/ Latino	M	75-79		● n										Lung, kidney	0	15	5 h 30 min
D32	—	Hispanic/ Latino	M	70-75		● n										Lung	1	27	4 h

**b** COVID-19 negative patients

Patient					Lung	Heart	Liver	Kidney	Spleen	Trachea	Lymph node	Muscle	Nasal scraping	Oral scraping	Brain	Organ failure	IMV (days)	S/s to death (days)	PMI (h, min)
<b>Hospital site B</b>																			
D22	White	Not Hispanic/ Latino	M	50-55	● s p											Multi-organ	1	3	20 h
D23	Black/ AA	Not Hispanic/ Latino	F	75-80	● s p											Heart	0	0	46 h
D24	White	Not Hispanic/ Latino	M	50-55	● s p											Multi-organ	2	5	43 h

● s, Spatial analysis; ● n, snRNA-Seq; ● c, snRNA-Seq; ● p, Parenchyma; ● COVID-19 donor tissue; ● CTA; ● WTA; ● Protein



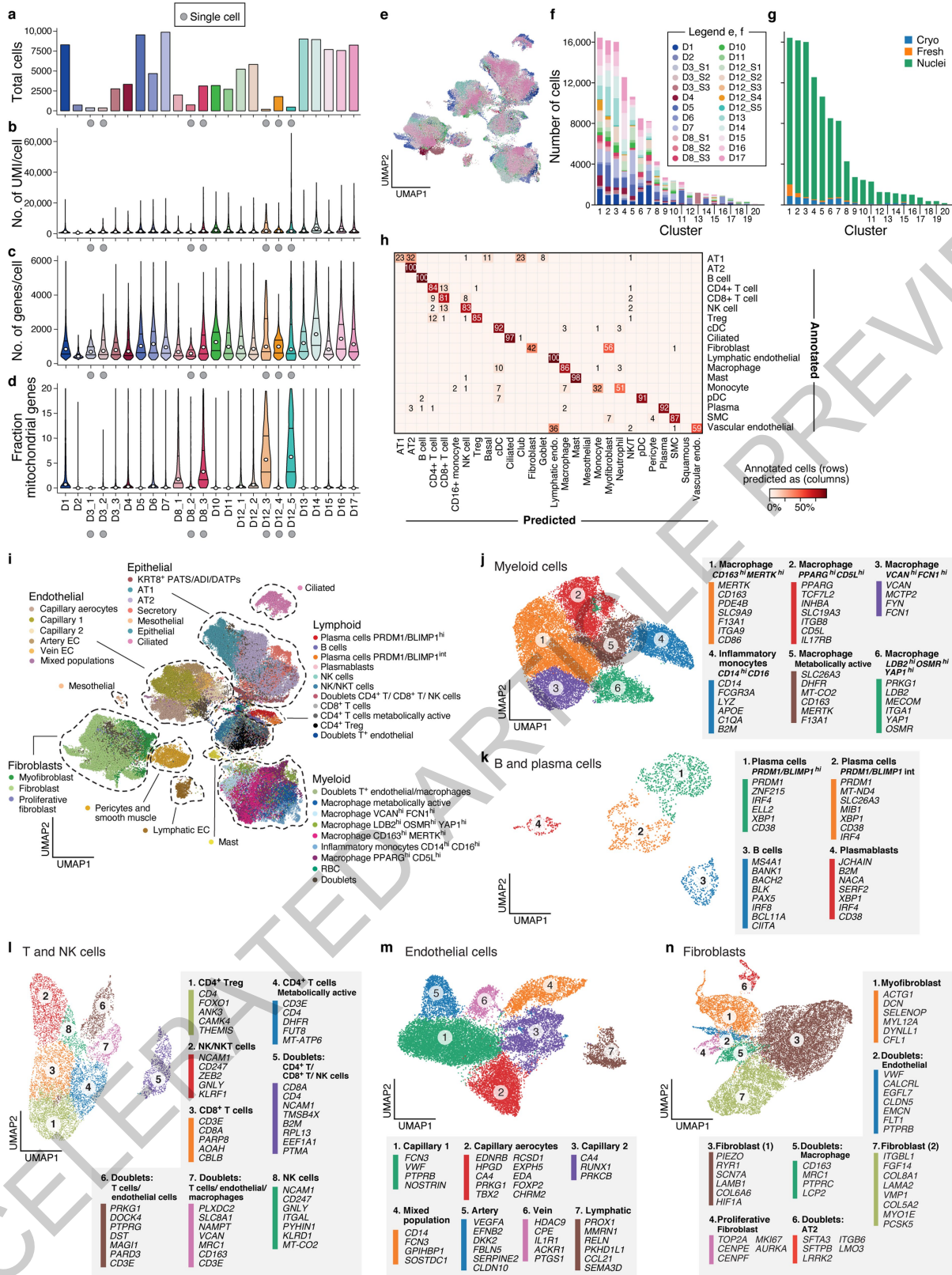
Extended Data Fig. 1 | See next page for caption.

## Article

**Extended Data Fig. 1 | A COVID-19 autopsy cohort, data quality and ambient RNA removal for a single cell/nucleus lung atlas. a.** COVID-19 cohort overview. IMV: intermittent mandatory ventilation days, S/s: time from symptom onset to death in days; PMI: post-mortem interval. **b-d.** Comparison of cell composition by scRNA-seq and snRNA-seq in matched samples. Proportion of cells ( $x$  axis) of each type (color code) in sc/snRNA-seq samples from the same three donors (D3, D8, D12). **e-h.** Cellbender 'remove-background' on a single sample (D1). **e.** CellBender improves cell clustering and expression specificity by removing ambient RNA and empty (non-cell) droplets. UMAP plot of snRNA-seq profiles (dots) either before (left) or after (right) CellBender processing, colored by clusters, with CellBender-determined empty droplets in black ( $k=2,508$  droplets removed,  $k=10,687$  cells

remaining). **f,g.** CellBender improves specificity of individual genes and cell type signatures. UMAP embedding of single nucleus profiles pre-CellBender (left) and post-CellBender (right) processing, colored by expression of the surfactant protein *SFTPA1* (**f**) or signature score (Scanpy's<sup>63</sup> `score_genes` function, color bar) for genes sets specific to lung AT2 (**g**) cells. Color bar saturation chosen to emphasize low expression. **h.** Improved specificity of surfactant gene expression with CellBender (same sample). Expression level ( $\log(\text{average UMI count per cell})$ , color) and percent of cells with nonzero expression (dot size) of surfactant genes (columns) across cell clusters (rows) before (left) and after (right) CellBender processing. Also shown, for comparison, are the results of an alternative method, DecontX (middle).

ACCELERATED ARTICLE PREVIEW



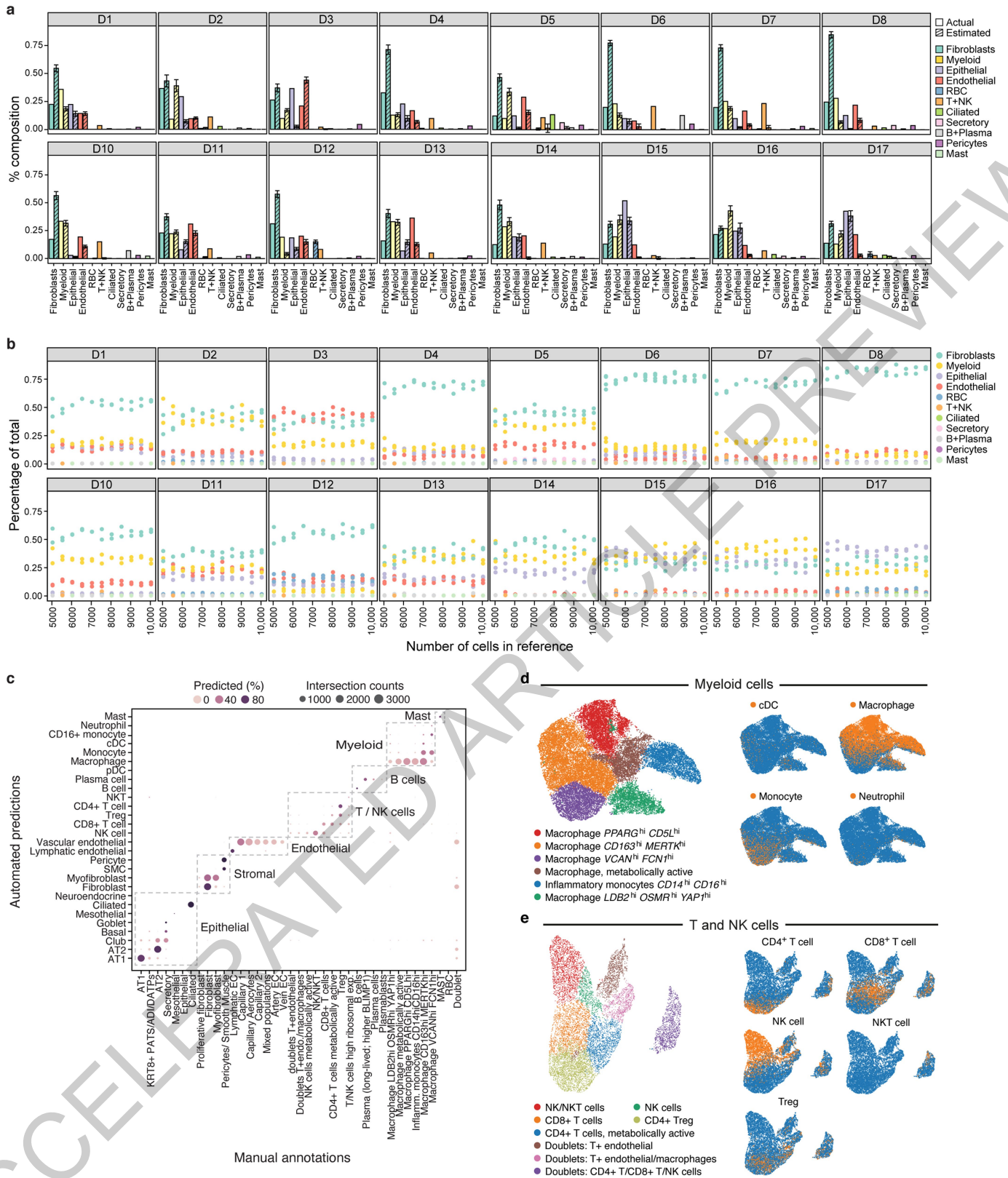
Extended Data Fig. 2 | See next page for caption.

## Article

**Extended Data Fig. 2 | Quality control and annotation in the COVID-19 lung cell atlas. a-d.** QC metrics for 24 lung samples (n=16 donors). Number of cells/nuclei (**a**, y axis) and distributions (median and first and third quartiles) of number of UMI per cell/nucleus (**b**, y axis), number of genes per cell/nucleus (**c**, y axis) and fraction of mitochondrial genes per cell/nucleus (**d**, y axis) across the samples (x axis) in the lung atlas. ScRNA-Seq samples are labeled by a grey circle. **e-g.** Cross-sample integration corrects batch effects. **e.** UMAP (as in Fig. 2a) of 106,792 sc/snRNA-Seq profiles post-Harmony<sup>65</sup> correction (Methods) colored by sample ID. **f,g.** Donors and processing protocols across clusters. Number of cells (y axis) from different donors (**f**) or processing protocols (**g**) in each Leiden cluster (x axis). **h.** Cross validation of automatic

annotation. Percent of cells (color bar) annotated in a class by Schiller *et al.*<sup>73</sup> that we predict for each class (columns). **i.** Identification of main lineage annotations by manual annotation. UMAP of 106,792 sc/snRNA-Seq profiles post-Harmony<sup>65</sup> correction (as in Fig. 2a) colored by manual annotation done in sub-clustering of each lineage. Dashed lines: chosen compartments for sub-clustering. **j-n.** Refined annotation of cell subsets within lineages. UMAP embeddings of each selected cell lineages with cells colored by manually annotated sub-clusters. Color legends highlight highly expressed marker genes for select subsets. **j.** myeloid cells ( $k=24,417$  cells/nuclei); **k.** B and plasma cells ( $k=1,693$ ); **l.** T and NK cells ( $k=9,950$ ); **m.** endothelial cells ( $k=20,366$ ); and **n.** fibroblast ( $k=20,925$ ).

ACCELERATED ARTICLE PREVIEW



Extended Data Fig. 3 | See next page for caption.



## Article

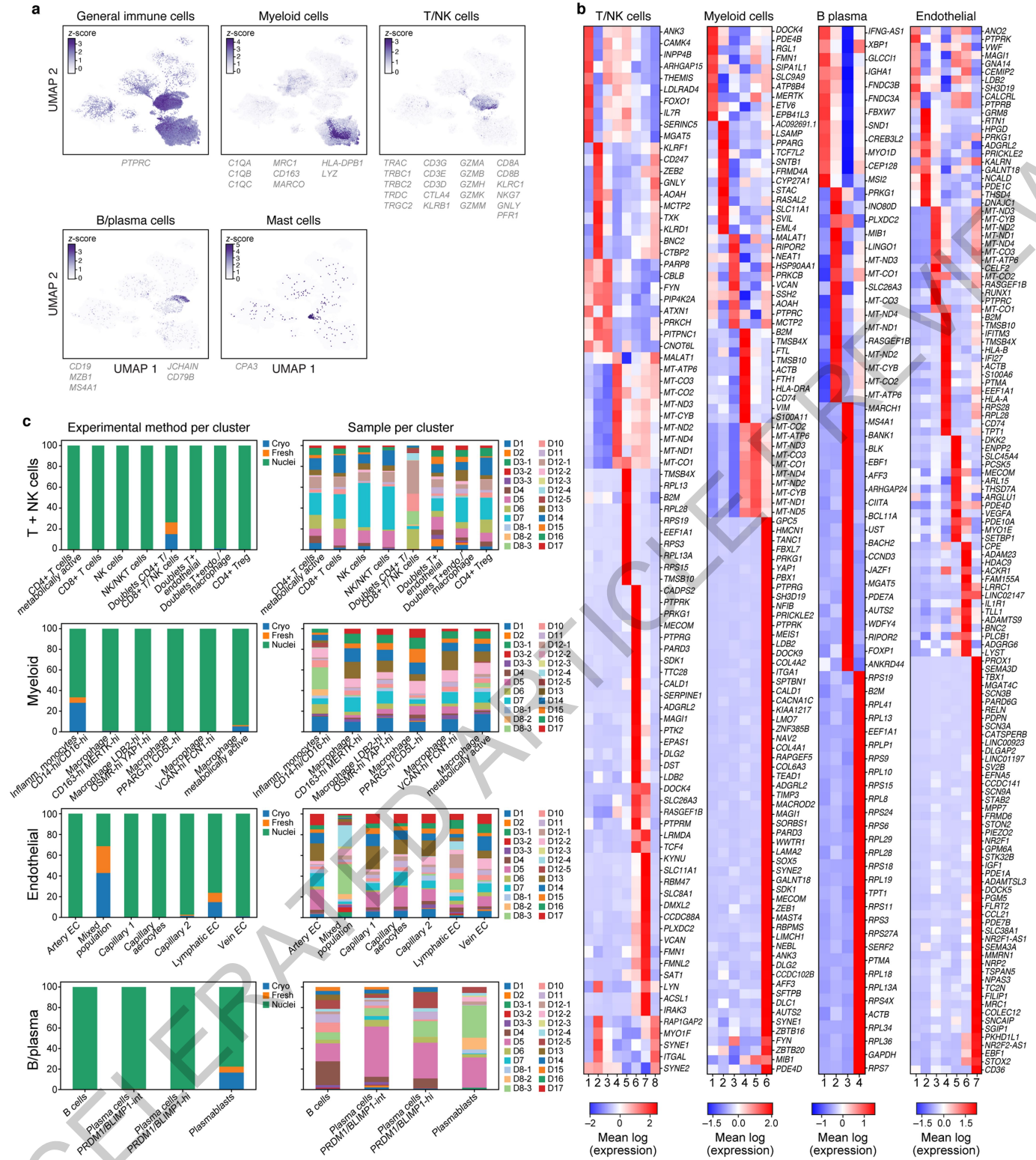
### Extended Data Fig. 3 | Bulk RNA-Seq deconvolution and comparison of automatic and manual annotations in the COVID-19 lung cell atlas.

**a,b.** Deconvolution of bulk RNA-Seq libraries from adjacent lung tissue.

**a.** Mean proportion (y axis, error bars = SD estimates from bulk RNA-Seq deconvolution (hatched bars; from MuSiC<sup>86</sup>) and from sc/snRNA-seq (filled bars) for each of 11 cell subsets (x axis) in each of 16 bulk RNA-Seq lung samples (panels) from 10 random samples of 10,000 cells each. **b.** Robustness of cell proportion estimates to the number of single cells sampled for the reference data. Mean proportion (y axis, from MuSiC) estimates for each of 11 cell subsets

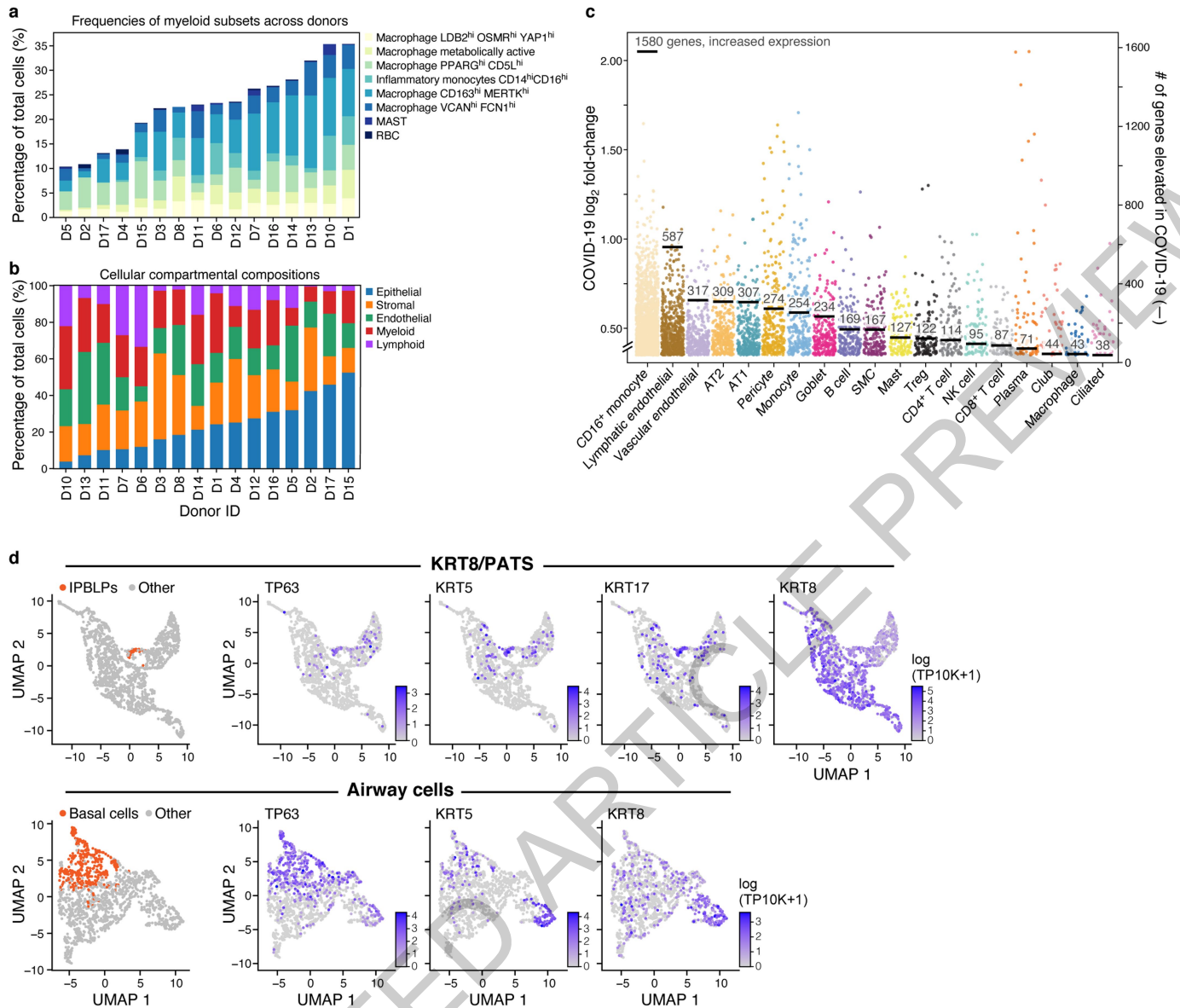
(color dots) in each of 16 bulk RNA-Seq lung samples (panels) when using three independent samples of 1,000 to 10,000 cells from the single cell reference (x axis). **c-e.** Agreement between automated and manual annotations. **c.** High consistency between automatic and manual annotations. The proportion (color intensity) and number (dot size) of cells with a given predicted annotation (rows) in each manual annotation category (columns). **d,e.** UMAP embedding of myeloid ( $k=24,417$  cells/nuclei) (**d**) and T and NK ( $k=9,950$  cells), (**e**) cell profiles colored by manually annotated subclusters (left) or automated predictions (right).

ACCELERATED ARTICLE PREVIEW



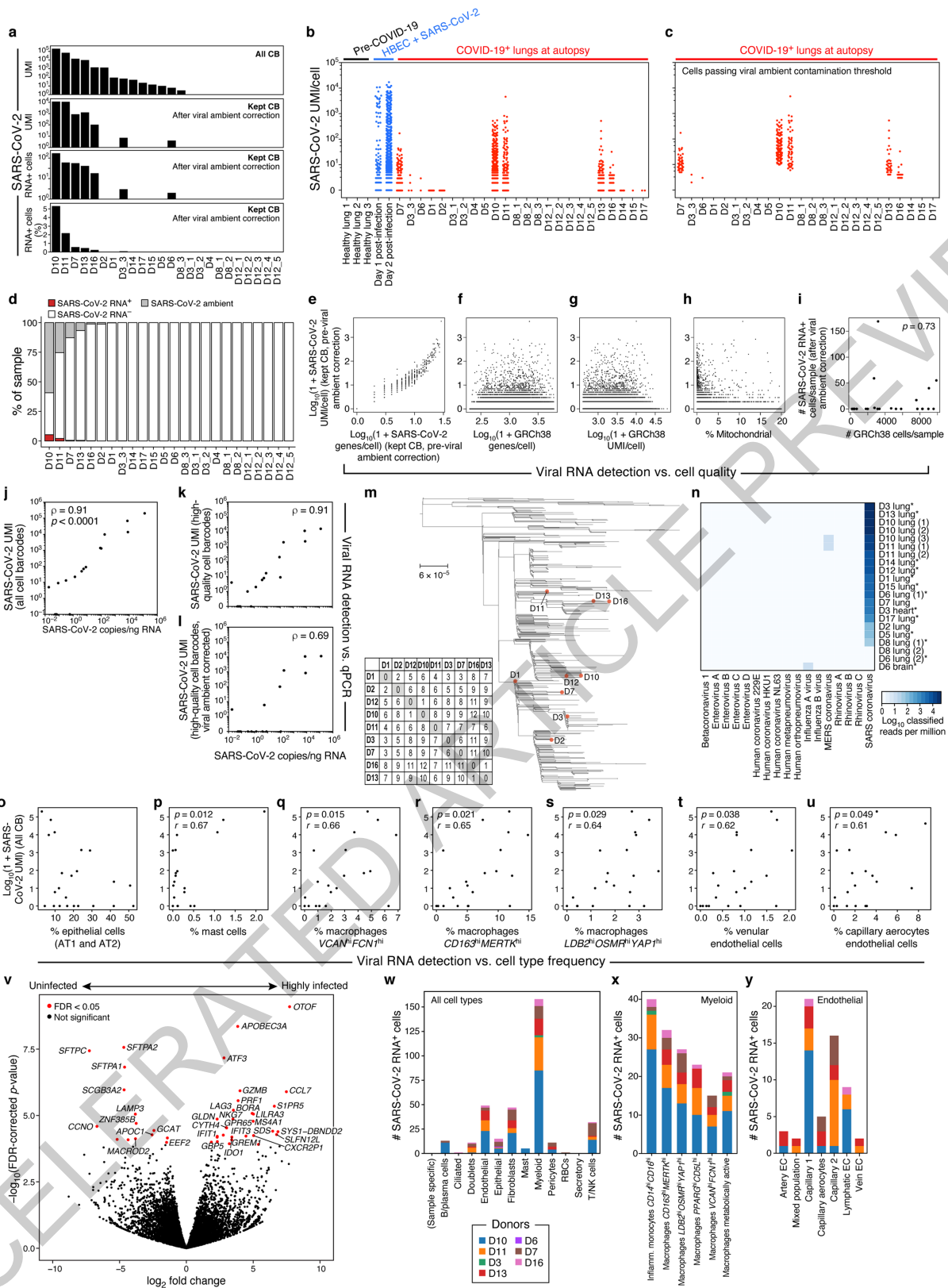
**Extended Data Fig. 4 | Manual annotation in the COVID-19 lung cell atlas.**  
**a, b.** Identification of main immune lineage annotations. **a.** UMAP of 106,792 sc/snRNA-Seq profiles post-Harmony correction (as in Fig. 2a) colored by expression of genes (color bar, genes listed below) used to separate immune cell sub-lineages (Methods). **b.** Differentially expressed genes between sub-clusters within each lineage. Expression (color bar) of genes (rows) that are differentially expressed (Methods) across the sub-clusters (columns) within

each compartment. DE genes shown are a union of the following: (i) top 10 DE genes between clusters, (ii) DE genes above an AUC of 0.8 and 0.75 for B/Plasma cells, (iii) pseudo-bulk DE genes above a log(fold change) threshold (thresholds: endothelial=4.2, T/NK=3, myeloid=4, B/plasma=2) (label on top). **c.** Batch correction within lineage. Fraction of cells/nuclei (y axis) from different processing protocols (left) or different donors (right, n=17) in each sub-cluster (x axis) after batch correction with Harmony<sup>63</sup> within each lineage.



**Extended Data Fig. 5 | Cell intrinsic programs and epithelial regenerative cell states in the COVID-19 lung cell atlas. a, b.** Differences in cell composition across donors. Percent of cells (y axis) from each myeloid subset (legend) in each donor (x axis). **b.** Percent of cells (y axis) from each main lineage (legend) in each donor (x axis), rank ordered by proportion of epithelial cells (blue). **c.** Myeloid, endothelial and pneumocyte cells show substantial changes in cell intrinsic expression profiles in COVID-19 lung. Log<sub>2</sub>(fold change) (y axis) between COVID-19 and healthy lung for each elevated gene (dot) in each

subset (x axis, by automatic annotation). Black bars: number of genes with significantly increased expression (adjusted p-value < 7.5\*10<sup>-6</sup>). Computed using a single cell based differential expression model applied to a meta-differential expression analysis between COVID-19 and healthy samples across 14 studies (see Methods). **d.** PATS and IBPLP cells in COVID-19 lung. UMAP embeddings of 1,550 KRT8<sup>+</sup> PATS-expressing cells (top) or of 1,394 airway epithelial cells (bottom) colored by IPBLPs or basal cells (orange, leftmost panels) or characteristic markers (purple, remaining panels).

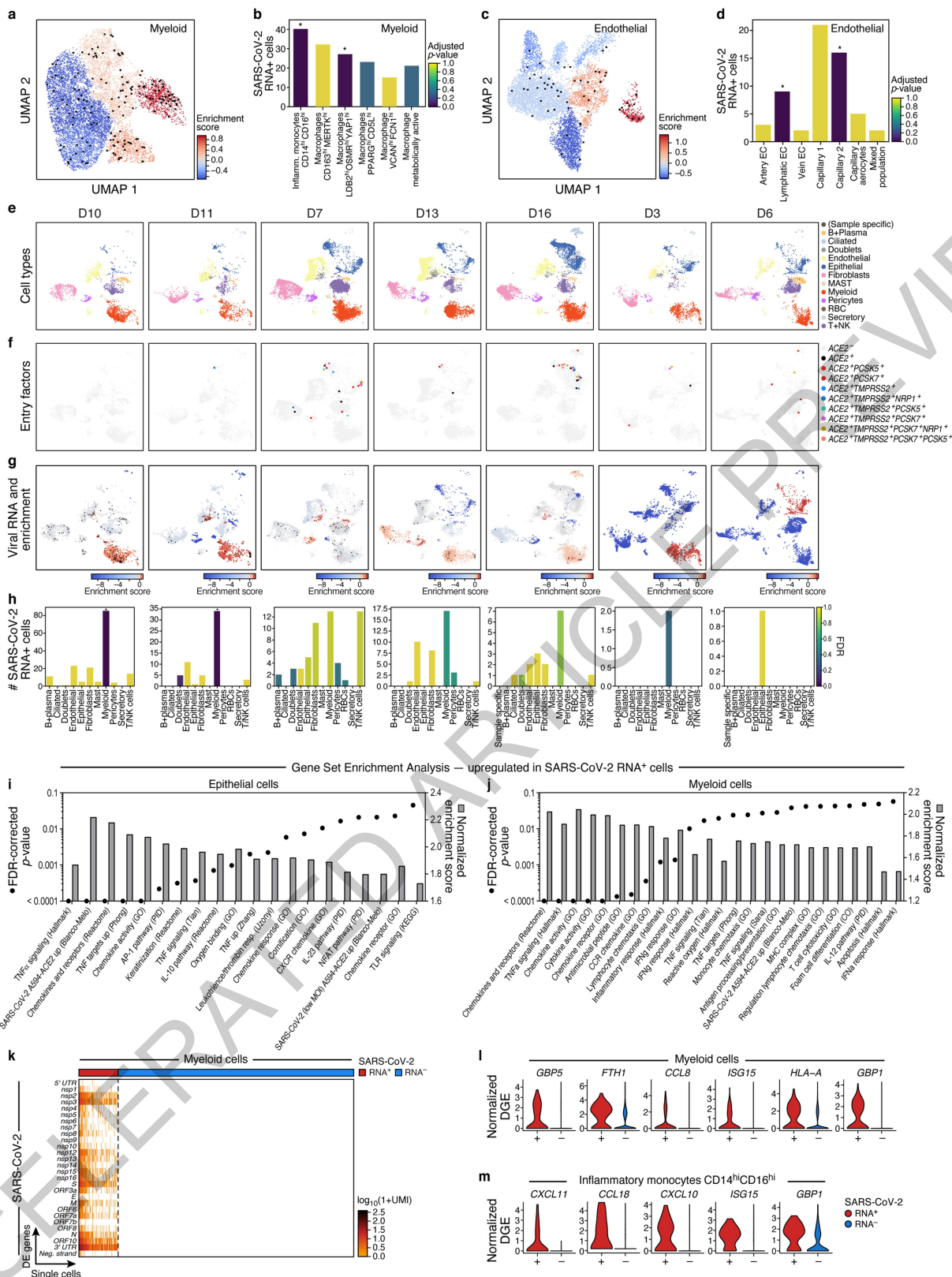


Extended Data Fig. 6 | See next page for caption.

# Article

**Extended Data Fig. 6 | SARS-CoV-2-RNA+ cells distinguished by sc/snRNA-Seq.** **a.** Detection of SARS-CoV-2 UMIs from sc/snRNA-Seq data. SARS-CoV-2 UMIs from all cell barcodes (top), and after ambient correction (second from top). Number (second from bottom) and percent (bottom) of SARS-CoV-2 RNA+ cells after ambient correction ( $m=24$  specimens). **b,c.** Impact of ambient RNA on SARS-CoV-2 RNA+ detection. Number of SARS-CoV-2 aligning UMI per Cell Barcode (CB) (y axis) in healthy lung (**b**, black), *in vitro* SARS-CoV-2 infected human bronchial epithelial cells (HBEC)<sup>110</sup> (**b**, blue) or lung samples from COVID-19 donors at autopsy either with CB with high-quality capture of human mRNA (**b**, red) or after removal of cells whose viral alignments were attributed to ambient contamination (**c**, Methods). **d.** Variation in SARS-CoV-2 RNA+ cells across donors. Percent of cells (y axis) assigned as SARS-CoV-2 RNA (white), SARS-CoV-2 RNA+ (red), or SARS-CoV-2 ambient (grey, Methods) across the donors (x axis), sorted by proportion of SARS-CoV-2 RNA+ cells. **e-i.** Viral RNA detection does not correlate with cell quality metrics. **e-h.** Number of SARS-CoV-2 UMIs (prior to ambient viral correction) for each cell (y axis) vs. either number of SARS-CoV-2 genes for that cell (**e**, x axis), number of human (GRCh38) genes per cell (**f**, x axis), number of human (GRCh38) UMI per cell (**g**, x axis), or % of human (GRCh38) mitochondrial UMIs per cell (**h**, x axis). **i.** Number of retained high-quality cells (x axis) and number of SARS-CoV-2 RNA+ cells (y axis) in each sample (dots) following correction for ambient viral reads. Pearson's  $r = 0.07$ , two-sided  $p = 0.73$ . **j-l.** Agreement in viral RNA detection between qPCR and sn/scRNA-Seq. Number of SARS-CoV-2 copies measured by CDC N1 qPCR on bulk RNA extracted from matched tissue samples (x axis) and the number of SARS-CoV-2 aligning UMI (y axis) for each

sample (dot) from all reads (**j**,  $p < 0.0001$ , two-sided), all reads from high-quality cell barcodes (**k**,  $p < 0.0001$ ), and after viral ambient RNA correction (**l**,  $p = 0.0042$ ). Spearman's  $\rho$  reported, two-sided test. **m.** Genetic diversity of SARS-CoV-2. Maximum likelihood phylogenetic tree of 772 SARS-CoV-2 genomes from cases in Massachusetts between January-May 2020. Orange points: donors in this cohort. **n.** Specificity of SARS-CoV-2 infection.  $\log_{10}(1+\text{reads})$  in each donor (columns) assigned to different viruses (rows) by metagenomic classification using Kraken2 from bulk RNA-Seq. Asterisks denote targeted capture. **o-u.** Relation between SARS-CoV-2 RNA and different cell types. Number of SARS-CoV-2 aligning UMIs in each (including all CB) and the proportion of epithelial (**o**), mast (**p**), macrophage  $VCAN^{\text{high}}FCN1^{\text{high}}$  (**q**), macrophages  $CD163^{\text{high}}MERTK^{\text{high}}$  (**r**), macrophages  $LDB2^{\text{high}}OSMR^{\text{high}}YAP1^{\text{high}}$  (**s**), venular endothelial (**t**) or capillary aerocytes (**u**) cells in these samples (x axes). Pearson's  $r$  denoted in the upper left corner with significance following Bonferroni correction ( $p$ ). **v.** Impact of viral load on bulk RNA profiles. Significance ( $-\log_{10}(P\text{-value})$ , y axis) and magnitude ( $\log_2(\text{fold-change})$ , x axis) of differential expression of each gene (dots) between three donors with highest viral load and six donors with lowest/undetectable viral load profiled by bulk RNA-Seq. Red points:  $FDR < 0.05$ . **w-y.** Distribution of SARS-CoV-2 RNA+ cells across cell types and subsets. Number of SARS-CoV-2 RNA+ cells (y axis) from each donor (color) across major categories (**w**, x axis), myeloid subsets (**x**, inflammatory monocytes: 40 cells, 5 donors;  $LDB2^{\text{high}}OSMR^{\text{high}}YAP1^{\text{high}}$  macrophages: 27 cells, 5 donors; x axis), or endothelial subsets (**y**, capillary endothelial cells: 16 cells, 4 donors; lymphatic endothelial cells: 9 cells, 3 donors; 16 cells, 4 donors, x axis).



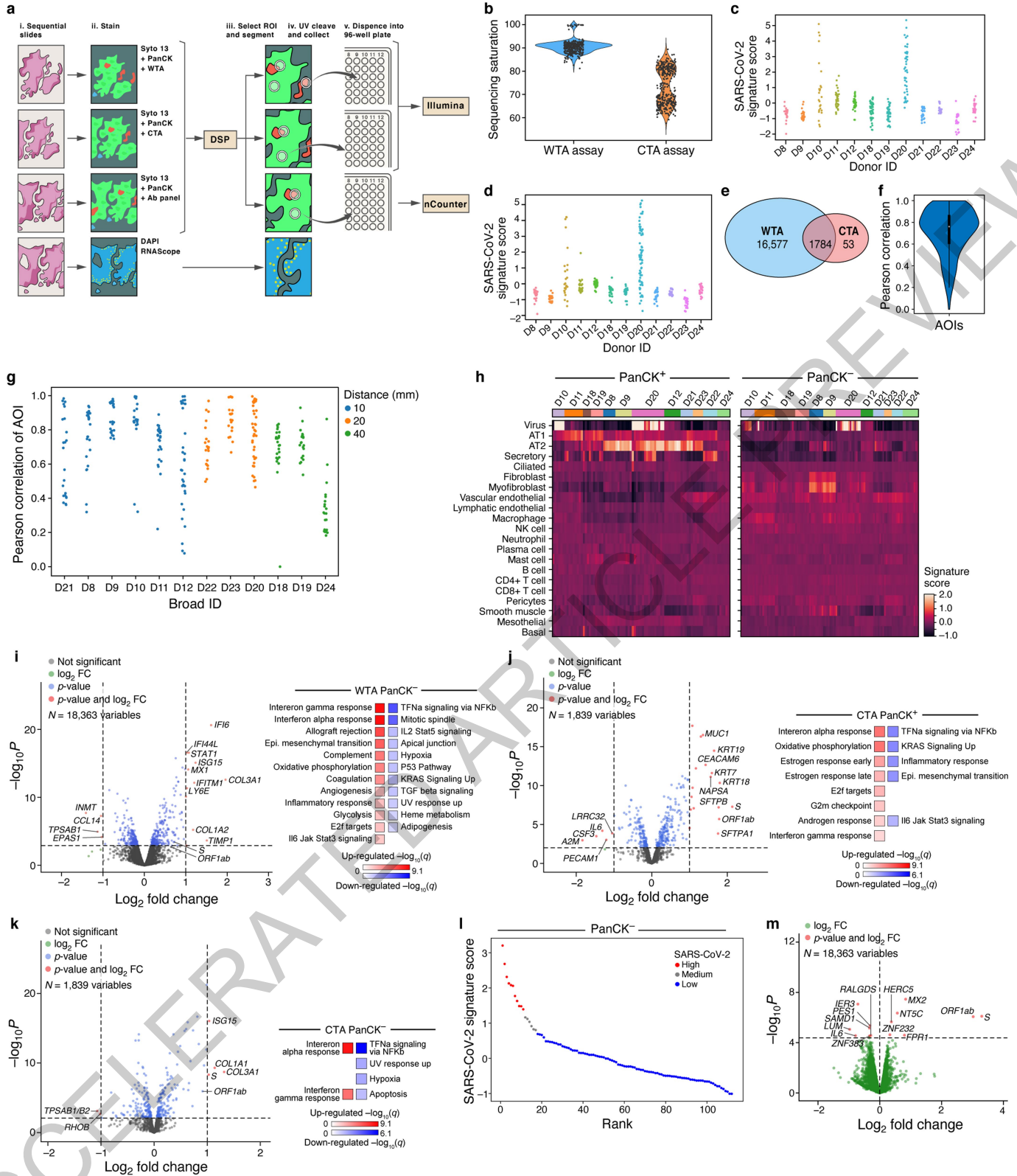
Extended Data Fig. 7 | See next page for caption.

## Article

**Extended Data Fig. 7 | Donor-specific enrichment of SARS-CoV-2 RNA+ cells and host responses to viral RNA. a-d.** SARS-CoV-2 RNA+ cells are enriched in specific lineages and sub-types. **a,c.** UMAP embeddings of either myeloid cells (**a**), or endothelial cells (**c**) from seven donors containing any SARS-CoV-2 RNA+ cell, and colored by viral enrichment score (color bar; red: stronger enrichment) and by SARS-CoV-2 RNA+ cells (black points). **b,d.** Number of SARS-CoV-2 RNA+ cells (y axis) per cell type/subset (x axis) in myeloid (**b**) or endothelial (**d**) subsets. Bar color: FDR (dark blue: higher significance, Methods; \* FDR < 0.05.). **b, e-h.** Variation across donors. **e-g.** UMAP embeddings of sc/snRNA-seq profiles from each of seven donors containing any SARS-CoV-2 RNA+ cell (columns), colored by major cell categories (**e**), expression of SARS-CoV-2 entry factors (**f**), or SARS-CoV-2 RNA enrichment per cluster (**g**, red/blue colorbar; red: high enrichment; black points: SARS-CoV-2 RNA+ cells). **h.** Number of

SARS-CoV-2 RNA+ cells (y axis) across major cell types (x axis) from each of seven donors containing any SARS-CoV-2 RNA+ cell (columns). Bar color: FDR (dark blue: higher significance). \* FDR < 0.05. **i,j.** Normalized enrichment score (bars, right y axis) and significance (points, FDR, left y axis) (by GSEA<sup>39,40</sup>, Methods) of different functional gene sets (x axis) in genes upregulated in SARS-CoV-2 RNA+ epithelial (**i**) or myeloid (**j**) cells. **k.** Expression of SARS-CoV-2 genomic features (log-normalized UMI counts; rows) across SARS-CoV-2 RNA+ ( $k=158$  cells) and SARS-CoV-2 RNA- ( $k=790$ ) myeloid cells (columns). **l,m.** Distribution of normalized expression levels (y axis) for select significantly differentially expressed genes between SARS-CoV-2 RNA- and SARS-CoV-2 RNA+ cells from all myeloid cells or Inflammatory monocytes  $CD14^{\text{high}}CD16^{\text{high}}$  cells.

ACCELERATED ARTICLE PREVIEW



Extended Data Fig. 8 | See next page for caption.



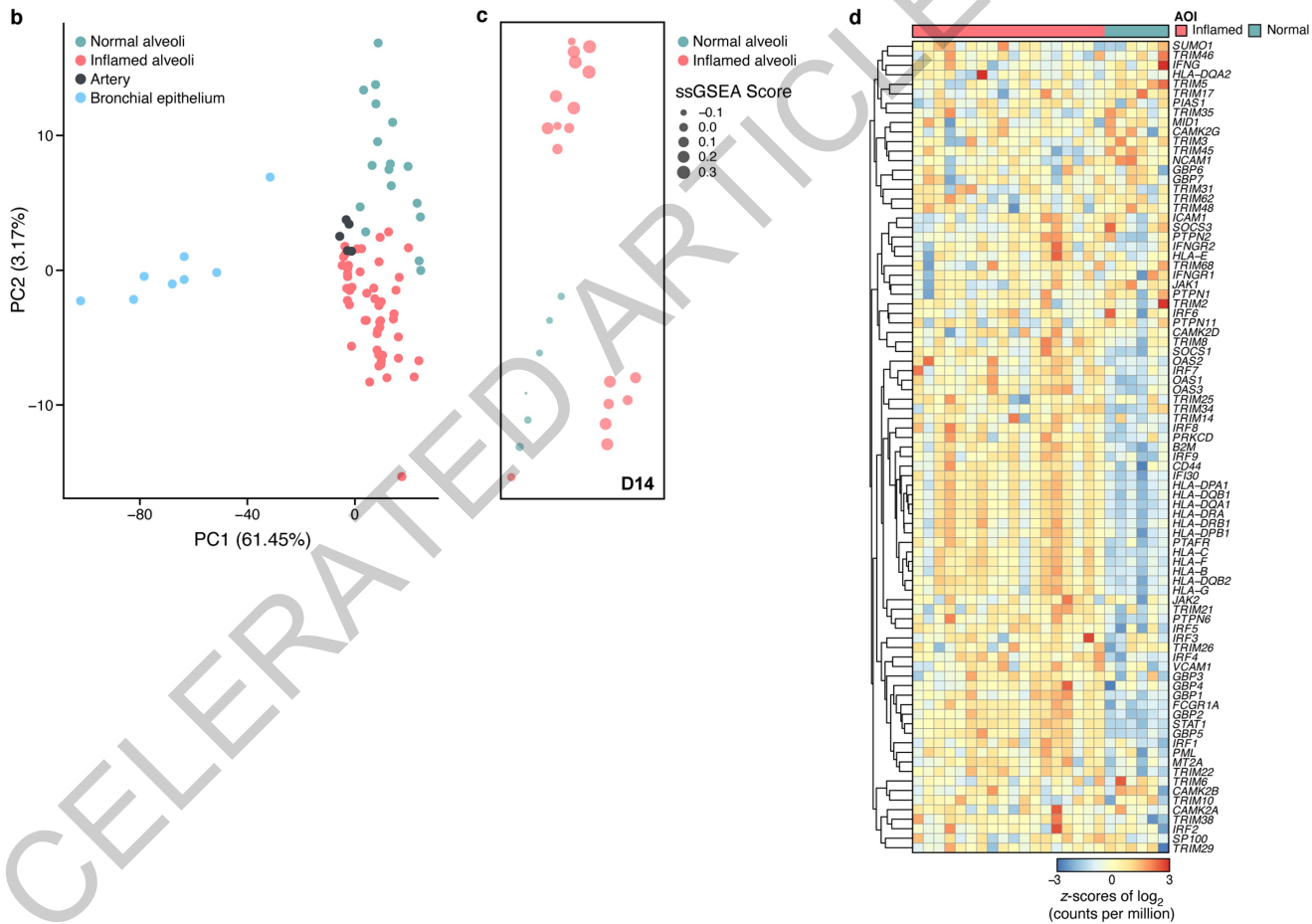
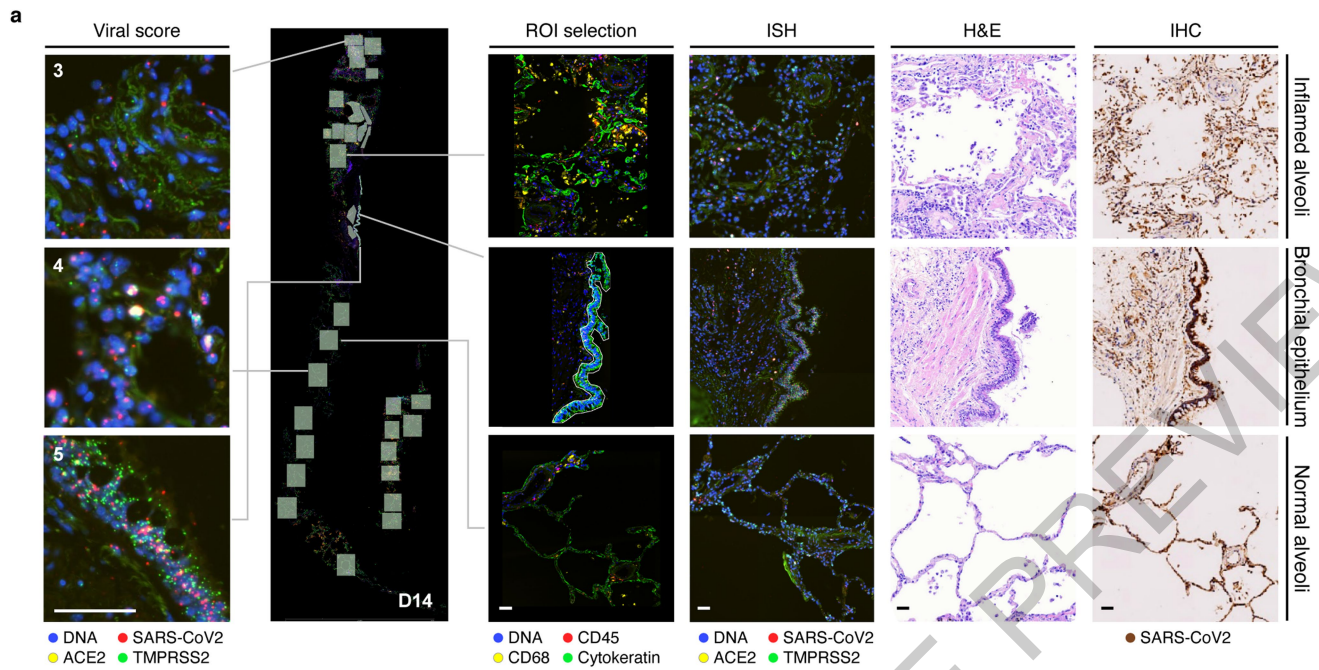
## Article

### Extended Data Fig. 8 | NanoString GeoMx experiment design and analysis.

**a.** Overview of spatial profiling experiments. **b.** Distribution of sequencing saturation (y axis, %) for WTA and CTA AOIs (x axis). **c,d.** SARS-CoV-2 signature score (y axis) for each WTA (**c**) and CTA (**d**) AOI (dots) from each donor (x axis). **e.** Overlap of WTA and CTA genes. **f,g.** Agreement between WTA and CTA. **f.** Distribution (box: interquartile range, white point: median, violin range: min-max) of Pearson correlation coefficients (y axis) between WTA and CTA profiles (for common genes across 296 AOIs). **g.** Pearson correlation coefficient (y axis) of WTA and CTA common genes for each AOI pair (dot) from each donor (x axis), sorted by distance between WTA and CTA sections (blue, 10 mm; orange, 20 mm; green, 40 mm). **h.** Cell composition differences between PanCK<sup>+</sup> and PanCK<sup>-</sup> alveolar AOIs and between AOIs from COVID-19 (n=9, 161 AOIs) and healthy (D22-24, 40 AOIs) lungs. Expression scores (color bar) of cell type signatures (rows) in PanCK<sup>+</sup> (left) and PanCK<sup>-</sup> (right) alveolar AOIs (columns) in CTA data from different donors (top color bar). **i-k.** Differential

gene expression in COVID-19 *vs.* healthy lung. Left: Significance ( $-\log_{10}$  (p-value), y axis) and magnitude ( $\log_2$ (fold-change), x axis) of differential expression of each gene (dots) in WTA for PanCK<sup>+</sup> (**i**, 112 COVID-19 *vs.* 20 healthy), and in CTA for PanCK<sup>+</sup> (**j**, 69 COVID-19 *vs.* 18 healthy) and PanCK<sup>-</sup> (**k**, 92 COVID-19 *vs.* 22 healthy) alveoli. Horizontal dashed line: FDR = 0.05, vertical dashed lines:  $|\log_2(\text{fold-change})| = 2$ . Right: Significance ( $-\log_{10}$  (q-value)) of enrichment (permutation test) of different pathways (rows). **l,m.** Changes in gene expression in SARS-CoV-2 high *vs.* low AOIs within COVID-19 lungs in WTA data. **l.** PanCK<sup>-</sup> alveolar AOIs (dots) rank ordered by their SARS-CoV-2 signature score (y axis) in WTA data, and partitioned to high (red), medium (grey) and low (blue) SARS-CoV-2 AOIs. **m.** Significance ( $-\log_{10}$ (p-value), y axis) and magnitude ( $\log_2$ (fold-change), x axis) of differential expression of each gene (dots) in WTA data between SARS-CoV-2 high and low AOIs for PanCK<sup>-</sup> alveoli (ROIs: 11 high, 6 medium, 95 low). Horizontal dashed line: FDR = 0.05.

ACCELERATED ARTICLE PREVIEW



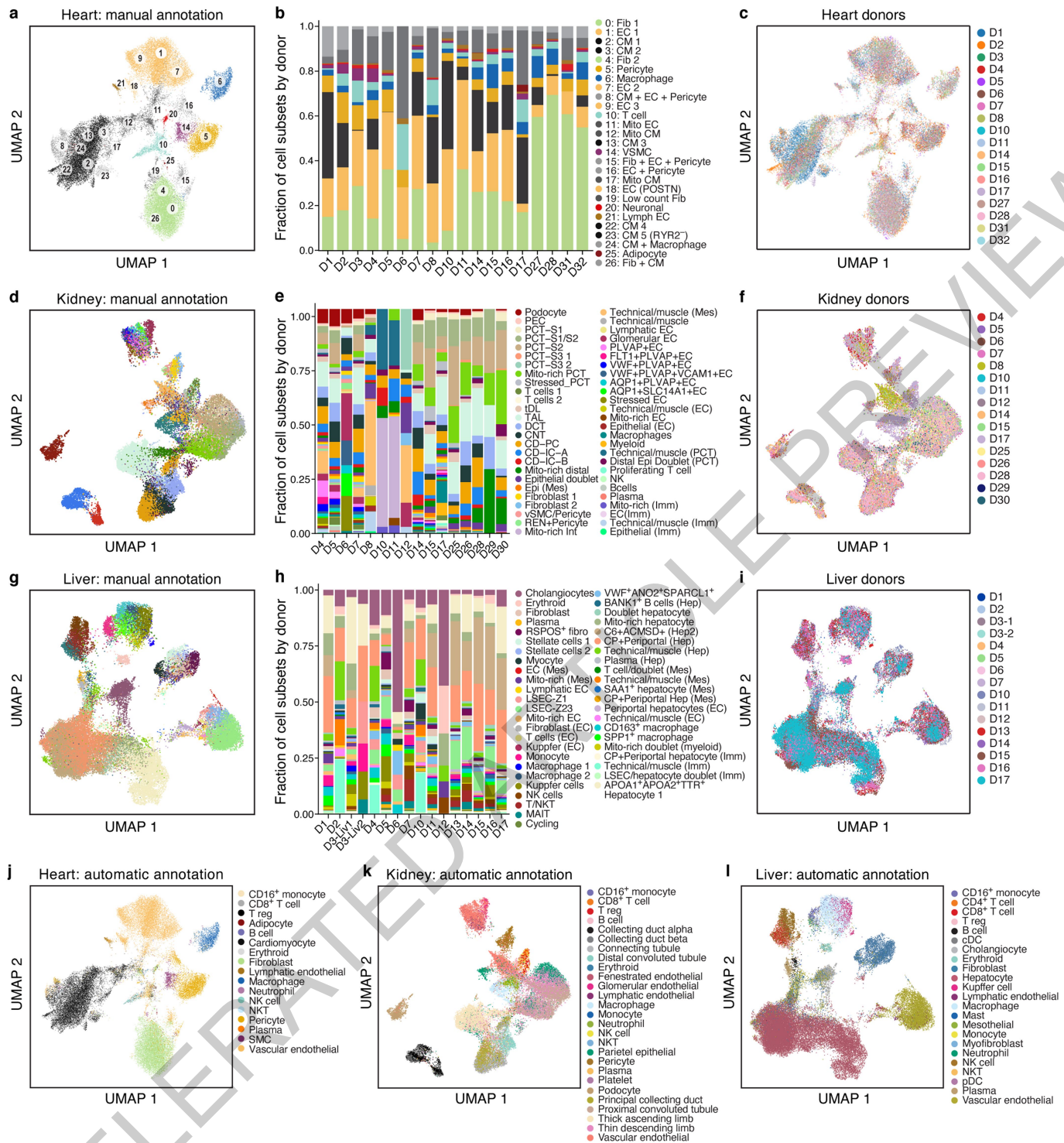
Extended Data Fig. 9 | See next page for caption.

## Article

**Extended Data Fig. 9 | GeoMx WTA DSP analysis of lung biopsies reveals region- and inflammation-specific expression programs.** **a.** Region selection. Serial sections of lung biopsies (five donors, D13-17; image depicts serial sections of D14) processed with GeoMx WTA-DSP with 4-color staining (DNA, *CD45*, *CD68*, PanCK), RNAscope with probes against (SARS-CoV-2 S-gene (utilized to derive semi-quantitative viral load scores), *ACE2*, *TMPRSS2*), H&E staining, and immunohistochemistry with anti-SARS-CoV-2 S-protein. Scale bar: 100  $\mu$ m. **b-d.** Regions and inflammation specific expression programs. **b.** The first two principal components (PCs, x and y axes) from lung ROI gene expression profiles from donors D13-17, spanning normal-appearing alveoli

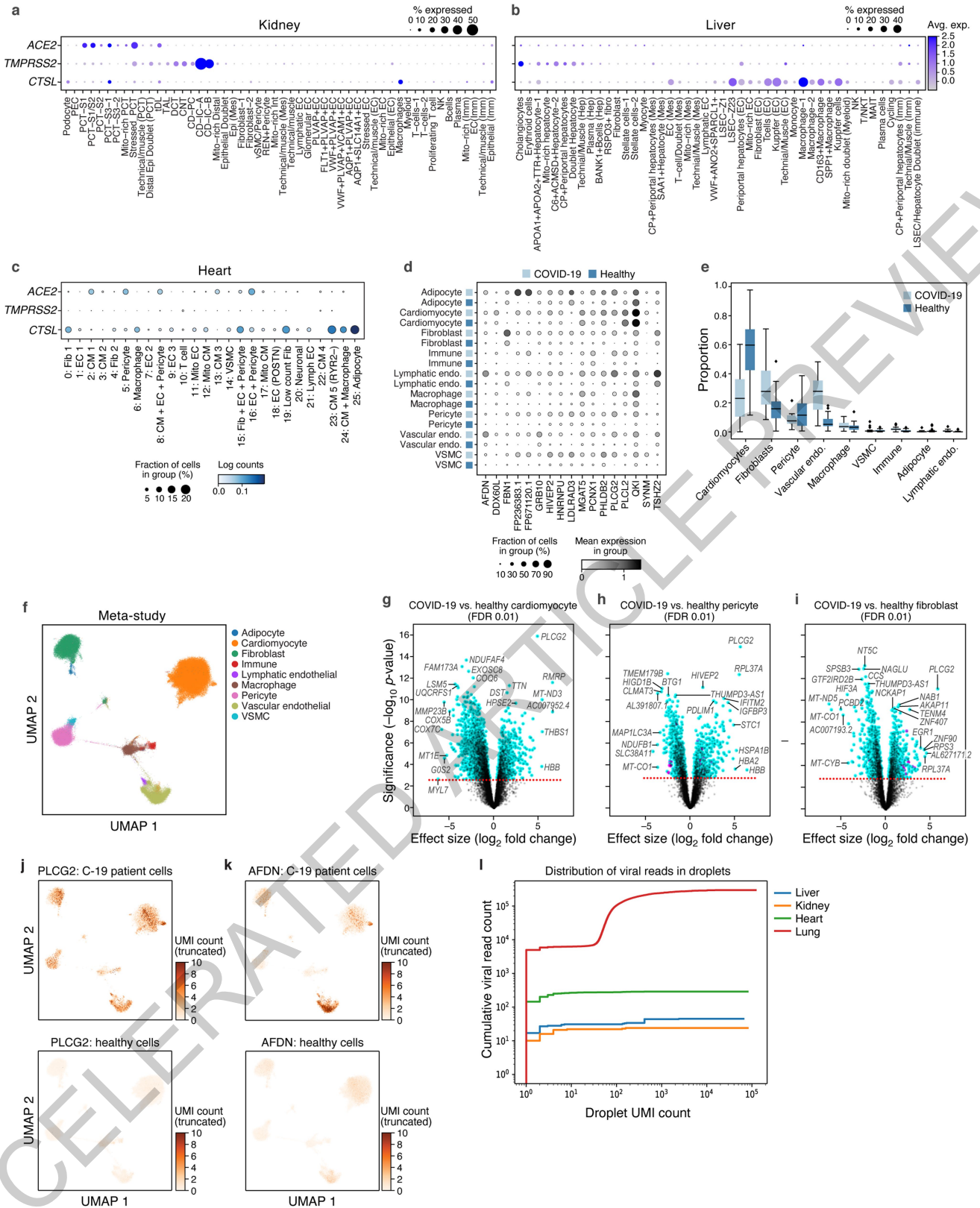
(green; D14=6 AOIs, D15=2 AOIs, D16=5 AOIs, D17=4 AOIs); inflamed alveoli (magenta; D13=14 AOIs, D14=18 AOIs, D15=7 AOIs, D16=3 AOIs, D17=8 AOIs); bronchial epithelium (blue; D14=2 AOIs, D15=1 AOI, D16=2 AOIs, D17=3 AOIs), and arterial blood vessels (black; D13=2 AOIs, D15=3 AOIs). **c.** GSEA score (circle size, legend) of the enrichment of the interferon- $\gamma$  pathway in each normal-appearing (green; 6 AOIs) and inflamed (magenta; 18 AOIs) alveolar AOIs (dot from the section of donor D14 (in **a**), placed in their respective physical coordinates on the tissue section (as in **a**)). **d.** Expression (color bar, log<sub>2</sub>(counts per million)) of IFN $\gamma$  pathway genes (rows) from normal-appearing (green, n=6) and inflamed alveoli (magenta, n=18) AOIs (columns) from D14 lung biopsy.

ACCELERATED ARTICLE PREVIEW



**Extended Data Fig. 10 | A single nucleus atlas of heart, kidney, and liver COVID-19 tissues.** a-c. COVID-19 heart cell atlas. UMAP embedding of 40,880 heart nuclei (dots) ( $n=18$  donors,  $m=19$  specimens) colored by Leiden resolution 1.5 clustering with manual *post hoc* annotations (a) or donors (c). b. Proportions of cells (y-axis) in each sample. d-f. COVID-19 kidney cell atlas. UMAP embedding of 33,872 kidney nuclei (dots) ( $n=16$ ,  $m=16$ ) colored by clustering with manual

*post hoc* annotations (d) or donors (f). e. Proportion of cells (y-axis) in each sample. g-i. COVID-19 liver cell atlas. UMAP embedding of 47,001 liver nuclei (dots) ( $n=15$ ,  $m=16$ ), colored by clustering with manual *post hoc* annotations (g) or donors (i). h. Proportion of cells (y-axis) in each sample. j-l. Automatic annotations. UMAP embeddings, colored by predicted cell type labels by automatic annotation for heart (j), kidney (k) and liver (l).

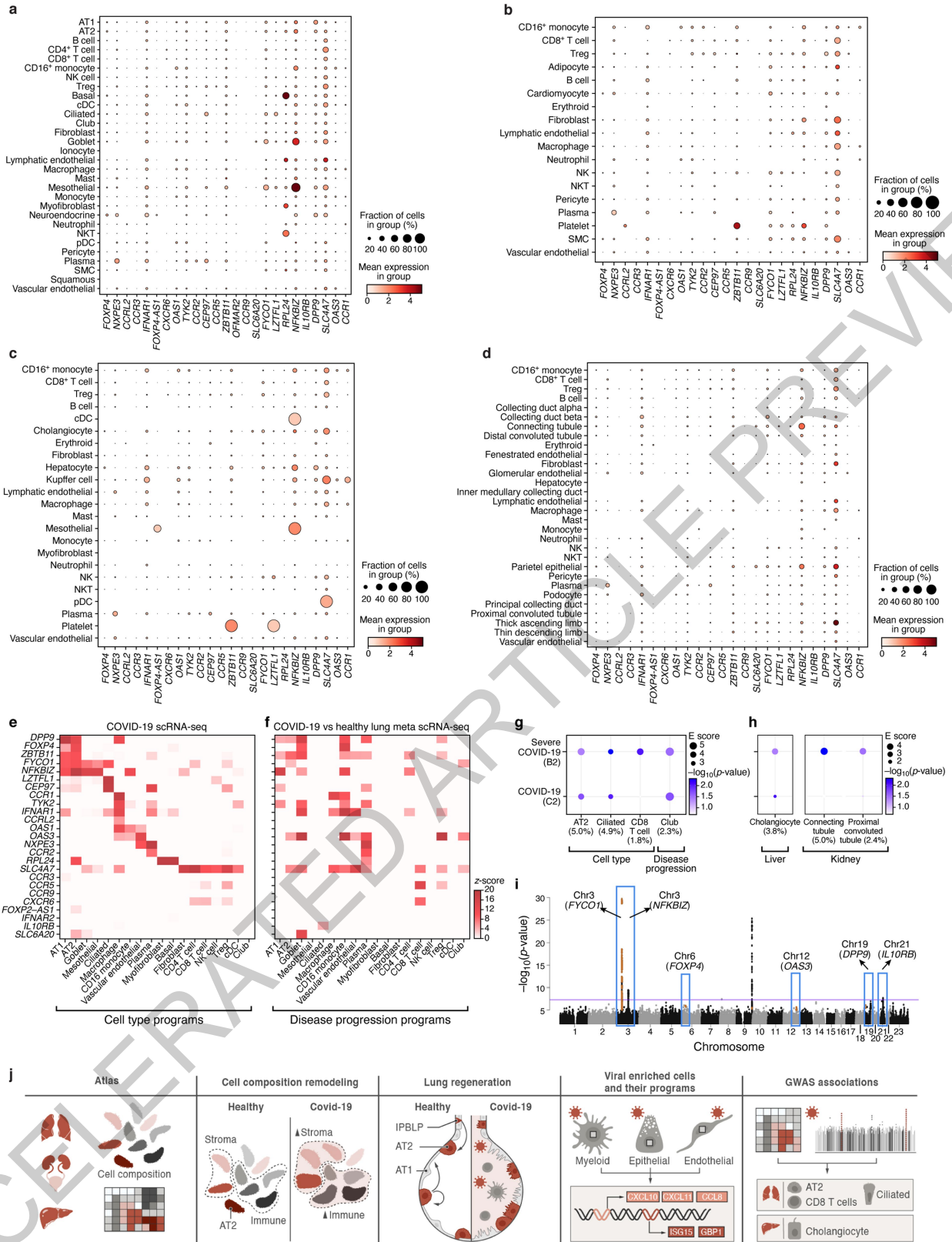


Extended Data Fig. 11 | See next page for caption.

**Extended Data Fig. 11 | Entry factors in heart, kidney and liver COVID-19 tissues and differential gene expression in heart cell atlas. a-c.** SARS-CoV-2 entry factors are expressed in kidney, liver, and heart cells. Average expression (dot color) and fraction of expressing cells (color, size) of SARS-CoV-2 entry factors (rows) across cell subsets (columns) in the kidney (**a**), liver (**b**), and heart (**c**). **d-k.** Genes and pathways differentially expressed between COVID-19 and healthy heart cells. **d.** Log mean expression per cell (dot color) and fraction of expressing cells (dot size) across cell types from healthy or COVID-19 heart (rows) for select genes (columns) that are differentially expressed between COVID-19 and healthy cells **e.** Proportions of each cell type for COVID-19 ( $n=15$ ) and healthy ( $n=28$ , 2 studies) samples (boxplots: middle line=mean, box bounds=first and third quartiles, whiskers=1.5x the interquartile range, minima=smallest observed proportion, maxima=highest observed proportion). **f.** UMAP embedding of integrated COVID-19 and healthy snRNA-seq profiles (dots) colored by major cell types. Plot limited to a subset of

151,373 high-quality cells for visualization purposes. **g-i.** Cell type specific differentially expressed genes in COVID-19 *vs.* healthy nuclei. Differential expression ( $\log_2(\text{fold change})$ , x axis), and associated significance ( $-\log_{10}(\text{P-value})$ , y axis, Methods) for each gene (dot) between COVID-19 *vs.* healthy nuclei of cardiomyocytes (**g**), pericytes (**h**), and fibroblasts (**i**). Dashed line: FDR=0.01. **j,k.** UMAP embedding of the meta-analysis atlas (as in **f**) but showing only COVID-19 (top) or healthy (bottom) nuclei profiles (dots) colored by expression of *PLCG2* (**j**) or *AFDN* (**k**). **l.** Low levels of viral UMIs in heart, liver and kidney, compared to lung. Cumulative viral read counts as a function of droplet UMI count. In lung (red) most viral-positive droplets are empty droplets (total UMI count - 100) with some viral-positive droplets which contain nuclei (UMI count > -1,000), but in heart (green), liver (blue), and kidney (orange), most of the "viral-positive" droplets have fewer than 10 total UMI counts, suggesting these reads are not trustworthy.

ACCELERATED ARTICLE PREVIEW



Extended Data Fig. 12 | See next page for caption.

**Extended Data Fig. 12 | Expression of GWAS curated genes across lung, heart, liver and kidney atlases. a-d.** Mean expression (dot color,  $\log(\text{TP10K} + 1)$ ) and proportion of expressing cells (dot size) for each of 26 curated GWAS implicated genes (columns) in each cell subset (rows) for lung (a), heart (b), liver (c) and kidney (d) COVID-19 autopsy atlases. Results only reported for genes with expression in at least one cell subset in the underlying tissue. Some GWAS genes have higher expression in the lung compared to the other three tissues. **e,f.** Mean expression (e, z-score relative to all other cell types, color bar) or differential expression (f, z-score of DE analysis of expression in COVID-19 vs. healthy cells of the same type) of 25 out of 26 GWAS implicated genes (rows) from 6 genomic loci associated with COVID-19 (based on summary statistics data from COVID-19 HGI meta analysis<sup>45</sup> across lung cell types (columns)). *ABO* was not considered as it was not reliably recovered in

scRNA-seq data. **g-h.** Cell type and disease progression gene programs in the lung (g), liver, and kidney (h) that contribute to heritability of COVID-19 severity. Magnitude (circle size, E score) and significance (color,  $-\log_{10}(\text{P-value})$ ) of the enrichment of cell type programs and cell-types specific disease programs (columns) that were significantly enriched for COVID-19 or severe COVID-19 phenotypes (rows). All results are conditional on 86 baseline- LDv2.1 model annotations. **i.** Nomination of single best candidate genes at unresolved GWAS significant loci by aggregating gene level information across program classes and cell types. Significance ( $-\log_{10}(\text{P-value})$ , y-axis) of GWAS association signal at locus (x-axis). Blue boxes: Significantly associated loci<sup>45</sup> at a genome-wide significance level (purple horizontal bar). **j.** Schematic summarizing the key findings and contributions of this study..

ACCELERATED ARTICLE PREVIEW



## Reporting Summary

Nature Research wishes to improve the reproducibility of the work that we publish. This form provides structure for consistency and transparency in reporting. For further information on Nature Research policies, see our [Editorial Policies](#) and the [Editorial Policy Checklist](#).

### Statistics

For all statistical analyses, confirm that the following items are present in the figure legend, table legend, main text, or Methods section.

n/a Confirmed

- The exact sample size ( $n$ ) for each experimental group/condition, given as a discrete number and unit of measurement
- A statement on whether measurements were taken from distinct samples or whether the same sample was measured repeatedly
- The statistical test(s) used AND whether they are one- or two-sided  
*Only common tests should be described solely by name; describe more complex techniques in the Methods section.*
- A description of all covariates tested
- A description of any assumptions or corrections, such as tests of normality and adjustment for multiple comparisons
- A full description of the statistical parameters including central tendency (e.g. means) or other basic estimates (e.g. regression coefficient) AND variation (e.g. standard deviation) or associated estimates of uncertainty (e.g. confidence intervals)
- For null hypothesis testing, the test statistic (e.g.  $F$ ,  $t$ ,  $r$ ) with confidence intervals, effect sizes, degrees of freedom and  $P$  value noted  
*Give  $P$  values as exact values whenever suitable.*
- For Bayesian analysis, information on the choice of priors and Markov chain Monte Carlo settings
- For hierarchical and complex designs, identification of the appropriate level for tests and full reporting of outcomes
- Estimates of effect sizes (e.g. Cohen's  $d$ , Pearson's  $r$ ), indicating how they were calculated

*Our web collection on [statistics for biologists](#) contains articles on many of the points above.*

### Software and code

Policy information about [availability of computer code](#)

Data collection

Data analysis

1. Terra, a Cloud platform for storing and sharing data and analysis, tools; <https://app.terra.bio/>
2. Cumulus/cellranger\_workflow on Cumulus, a (cloud-based) framework for running cellranger mkfastq and cellranger counts; used to run cellranger counts, version run was Snapshot 10 on Terra ;Read the Docs: <https://cumulus.readthedocs.io/en/latest/cellranger.html>; Terra WDL: [https://portal.firecloud.org/?return=terra#methods/cumulus/cellranger\\_workflow/10](https://portal.firecloud.org/?return=terra#methods/cumulus/cellranger_workflow/10)
3. SARS-CoV-2 genome , used to align viral reads. Transcriptome reference name: BetaCov/South Korea/KCDC03/2020 based on NC\_045512.2 <https://github.com/hyeshik/sars-cov-2-transcriptome>
4. Cumulus/cumulus workflow on Cumulus, a (cloud-based) framework for high-throughput single cell and single nucleus analysis using Pegasus; used for quality control and clustering analysis on individual samples, version run was Snapshot 29 on Terra; Read the Docs: <https://cumulus.readthedocs.io/en/latest/cumulus.html#>; Terra WDL: <https://portal.firecloud.org/?return=terra#methods/cumulus/cumulus/29>
5. CellBender remove-background, removes ambient RNA and other technical artifacts from count matrices, version 0.2.0. Read the Docs: <https://cellbender.readthedocs.io>; Terra WDL: cellbender/remove-background (snapshot 11) Terra WDL: <https://portal.firecloud.org/#methods/cellbender/remove-background/11>
6. Scanpy, Python package for scRNA-seq data handling/processing, version 1.5.1+1.5.2.dev5+ge5d246aa; <https://scanpy.readthedocs.io>
7. Harmony-Pytorch, Python implementation of Harmony batch correction method, version 0.1.3; <https://github.com/lilab-bcb/harmony-pytorch>
8. Pegasus, Python package for scRNA-seq data handling/processing and generating heatmaps for NanoString GeoMx data, version 0.17.2; 1.0.0; <https://pegasus.readthedocs.io>
9. DESeq2, R package for analysis differential gene expression, version 1.28.0 for bulk RNA seq analysis, version 1.30.0 for viral and spatial DE analysis <http://bioconductor.org/packages/release/bioc/html/DESeq2.html>
10. MuSiC, R package for estimation of cell type proportions in bulk RNA-seq data, version 0.1.1; <https://github.com/xuranw/MuSiC>
11. GSEA, software for analyzing gene set enrichments, version 4.1.0 (run with database available as of 11/1/2020); <https://www.gsea->

- msigdb.org/gsea/index.jsp
12. GeoMx NGS Pipeline (DND) Processing Nanostring GeoMx NGS data for WTA and CTA assays, version 1.0.0; [https://blog.nanostring.com/geomx-online-user-manual/Content/NGS\\_DND/Running\\_DND.htm#Running3](https://blog.nanostring.com/geomx-online-user-manual/Content/NGS_DND/Running_DND.htm#Running3)
  13. Limma, R package for differential gene expression analysis for NanoString GeoMx and heart snRNA-seq data, version 3.44.3; <http://bioconductor.org/packages/release/bioc/html/limma.html>
  14. edgeR, R package for differential gene expression analysis for NanoString GeoMx data, version 3.28.1 or higher; <https://bioconductor.org/packages/release/bioc/html/edgeR.html>
  15. EnhancedVolcano, R package for generating volcano plots for differential genes for analysis on NanoString GeoMx data, version 1.6.0; <https://bioconductor.org/packages/release/bioc/html/EnhancedVolcano.html>
  16. fgsea, R package for gene set enrichment analysis on NanoString GeoMx and heart snRNA-seq data, version 1.14.0; <http://bioconductor.org/packages/release/bioc/html/fgsea.html>
  18. Viral-ngs, a collection of pipelines for viral genomic analyses including genome assembly and metagenomic classification, version 2.0.21; <https://viral-ngs.readthedocs.io/en/latest/>; <https://dockstore.org/organizations/BroadInstitute/collections/pgs>
  19. Scikit-learn, Python module for machine learning, version 0.23; <https://scikit-learn.org/stable/>
  20. Statsmodels, Python module for statistical modeling version 0.12.1 <https://www.statsmodels.org/stable/index.html>
  21. Idsc, Python module for GWAS heritability analysis. <https://github.com/bulik/ldsc>
  22. MAGMA, C++ command line interface for gene-level GWAS analysis version 1.08b <https://ctg.cncr.nl/software/magma>
  23. scCODA, statistical testing for compositional analysis for scRNA-seq data , v0.1.1.post1, <https://github.com/theislabs/scCODA/releases/tag/0.1.1.post1>
  24. adjusted\_rand\_score from sklearn.metrics.cluster was used to compute rand index for sub-clustering. [https://scikit-learn.org/stable/modules/generated/sklearn.metrics.adjusted\\_rand\\_score.html](https://scikit-learn.org/stable/modules/generated/sklearn.metrics.adjusted_rand_score.html)
  25. DecontX, ambient RNA removal from scRNA-seq count matrix data (part of the “celda” package) <https://github.com/campbio/celda> version 1.5.11
  26. GSVA, R package for gene set enrichment analysis was used to estimate the ssGSEA score for the alveoli NanoString GeoMX data. <https://www.bioconductor.org/packages/release/bioc/html/GSVA.html>
  27. Seurat R package for snRNA-seq data analysis v3.2.1
  28. R packages ggplot2 v3.3.2, dplyr 0.8.0.1, reshape2 v1.4.3 and cowplot v1.1.0 for visualization
  29. liger R package v0.5.0 <https://github.com/welch-lab/liger> (Linked Inference of Genomic Experimental Relationships)
  30. RSEM for bulk RNA-seq analysis , v1.2.8. , <https://deweylab.github.io/RSEM/>
  31. STAR for bulk RNA-seq alignment, v2.6.0c , <https://github.com/alexdobin/STAR>

For manuscripts utilizing custom algorithms or software that are central to the research but not yet described in published literature, software must be made available to editors and reviewers. We strongly encourage code deposition in a community repository (e.g. GitHub). See the Nature Research [guidelines for submitting code & software](#) for further information.

## Data

Policy information about [availability of data](#)

All manuscripts must include a [data availability statement](#). This statement should provide the following information, where applicable:

- Accession codes, unique identifiers, or web links for publicly available datasets
- A list of figures that have associated raw data
- A description of any restrictions on data availability

### Data availability

Processed sequencing data (sc/snRNA-Seq and bulk) are available in the Gene Expression Omnibus (GEO, <https://www.ncbi.nlm.nih.gov/geo/>) under accession no. GSE171668 and raw human sequencing data is available in the controlled access repository DUOS (<https://duos.broadinstitute.org/>), under Dataset IDs DUOS-000126, DUOS-000127, DUOS-000128 and DUOS-000129. Viral genome assemblies and short-read sequencing data are publicly available on NCBI's Genbank and SRA databases, respectively, under BioProject PRJNA720544. GenBank accessions for SARS-CoV-2 genomes are MW885875-MW885883. Data for other tissues in the biobank will be released as they are acquired.

The processed data is available on the Single Cell Portal:

Lung - [https://singlecell.broadinstitute.org/single\\_cell/study/SCP1052/](https://singlecell.broadinstitute.org/single_cell/study/SCP1052/)  
 Heart - [https://singlecell.broadinstitute.org/single\\_cell/study/SCP1216/](https://singlecell.broadinstitute.org/single_cell/study/SCP1216/)  
 Kidney - [https://singlecell.broadinstitute.org/single\\_cell/study/SCP1214/](https://singlecell.broadinstitute.org/single_cell/study/SCP1214/)  
 Liver - [https://singlecell.broadinstitute.org/single\\_cell/study/SCP1213/](https://singlecell.broadinstitute.org/single_cell/study/SCP1213/)

Nanostring GeoMx raw and normalized count matrices are available on GEO under accession no. GSE163530. Raw images will be available upon request.

## Field-specific reporting

Please select the one below that is the best fit for your research. If you are not sure, read the appropriate sections before making your selection.

- Life sciences       Behavioural & social sciences       Ecological, evolutionary & environmental sciences

For a reference copy of the document with all sections, see [nature.com/documents/nr-reporting-summary-flat.pdf](https://nature.com/documents/nr-reporting-summary-flat.pdf)

## Life sciences study design

All studies must disclose on these points even when the disclosure is negative.

Sample size

We generated sc/snRNA-Seq atlases of:

Sample size	<p>lung (n=16 donors, k=106,792 cells/nuclei, x=23 specimens; Donors=D1-8, 10-17) heart (n=18, k=40,880, x=19 specimens, D1-8, 10-11,14-17, 27-28, 31-32) liver (n=15, k=47,001, x=16 specimens; D1-7,10-17) kidney (n=16, k= 33,872, x=16 specimens;D4-8,10-12,14-15,17,25-26,28-30)</p> <p>We generated spatial data on the following: lung(n= 17 donors, x= 17 samples, Donors=D8-17,22-24) heart(n=1 donor, x= 1 sample, Donor =D20) heart(n=1 donor, x= 1 sample, Donor =D20)</p> <p>Because these are samples from human COVID-19 autopsy donors, we collected samples from as many donors that would consent over the collection period. We did not perform any power analyses prior to this.</p>
Data exclusions	CellBender was used to remove ambient RNA and other technical artifacts from the count matrices. Following CellBender, individual samples were processed using Cumulus, including filtering out cells/nuclei with fewer than 400 UMI, 200 genes, or greater than 20% of UMIs mapped to mitochondrial genes.
Replication	These are samples from human COVID-19 autopsy donors, so we could not replicate samples
Randomization	These are samples from human COVID-19 autopsy donors, so we could not randomize
Blinding	These are samples from human COVID-19 autopsy donors, so this was not applicable to our study

## Reporting for specific materials, systems and methods

We require information from authors about some types of materials, experimental systems and methods used in many studies. Here, indicate whether each material, system or method listed is relevant to your study. If you are not sure if a list item applies to your research, read the appropriate section before selecting a response.

### Materials & experimental systems

n/a	Involved in the study
<input type="checkbox"/>	<input checked="" type="checkbox"/> Antibodies
<input checked="" type="checkbox"/>	<input type="checkbox"/> Eukaryotic cell lines
<input checked="" type="checkbox"/>	<input type="checkbox"/> Palaeontology and archaeology
<input checked="" type="checkbox"/>	<input type="checkbox"/> Animals and other organisms
<input type="checkbox"/>	<input checked="" type="checkbox"/> Human research participants
<input checked="" type="checkbox"/>	<input type="checkbox"/> Clinical data
<input checked="" type="checkbox"/>	<input type="checkbox"/> Dual use research of concern

### Methods

n/a	Involved in the study
<input checked="" type="checkbox"/>	<input type="checkbox"/> ChIP-seq
<input checked="" type="checkbox"/>	<input type="checkbox"/> Flow cytometry
<input checked="" type="checkbox"/>	<input type="checkbox"/> MRI-based neuroimaging

## Antibodies

Antibodies used	<p>Immune Cell Profiling Panel (Core); Nanostring Inc; GMX-PROCONCT-HICP-12, Item 121300101, Lot# 0474026 IO Drug Target Panel; GMX-PROMODNCT-HIODT-12, Item 121300102, Lot# 0474029 Immune Activation Status Panel; Nanostring Inc; GMX-PROMODNCT-HIAS-12, Item 121300103, Lot# 0474032 Immune Cell Typing Panel; Nanostring Inc; GMX-PROMODNCT-HICT-12, Item 121300104, Lot# 0474035 Cell Death Panel; Nanostring Inc; GMX-PROMOD-NCTHCD-12, Lot# 0474050 MAPK Signaling Panel; Nanostring Inc; GMX-PROMOD-NCTHMAPK-12, Lot# 0474047 PI3K/AKT Signaling Panel; Nanostring Inc; GMX-PROMOD-NCTHPI3K-12, Lot# 0474053 Covid-19 GeoMx-formatted Antibody Panel including (TMPRSS2, clone EPR3861; ACE2, clone EPR4436; Cathepsin L/V/K/H, clone EPR8011; DDX5, clone EPR7239; and SARS-CoV-2 spike glycoprotein, polyclonal) ; Abcam; ab273594, Lot# GR3347471-1 GeoMx Solid Tumor TME Morphology Kit; Nanostring Inc; GMX-PRO-MORPH-HST-12; Item 121300310 Alexa Fluor® 647 alpha-Smooth Muscle Actin Antibody, clone 1A4 ; Novus Bio; IC1420R CD68 antibody, KP1 clone from Santa Cruz (sc-20060 AF594)</p>
Validation	<p>Nanostring morphological and staining panels are pre-validated by the manufacturer: <a href="https://www.nanostring.com/wp-content/uploads/2020/12/GeoMx_Antibody_Validation_White_Paper-3.pdf">https://www.nanostring.com/wp-content/uploads/2020/12/GeoMx_Antibody_Validation_White_Paper-3.pdf</a> Morphological markers were previously demonstrated in human tissue in <a href="https://doi.org/10.1101/2020.08.25.267336">https://doi.org/10.1101/2020.08.25.267336</a></p>

## Human research participants

Policy information about [studies involving human research participants](#)

Population characteristics	Extended Data Table 1 - Patient metadata table
Recruitment	For BWH: Subjects were recruited who had died with positive SARS-CoV-2 NP swab test prior to death, and were consented for autopsy to be performed at BWH less than 24 hours from the time of death. No decisions were influenced by subject age,

race/ethnicity, sex/gender, pre-mortem treatments, or co-morbidities.

For MGH: All patients at the Massachusetts General Hospital (MGH) who succumbed from SARS-CoV-2 infection, as confirmed by the qRT-PCR assays performed on nasopharyngeal swab specimens, were eligible for clinical autopsy upon consent by their healthcare proxy or next of kin. A subset of these patients were also enrolled in the MGH Rapid Autopsy Protocol if they had a history of known or suspected malignancy. Their clinical data and research specimens were collected in accordance with Dana Farber/Harvard Cancer Center Institutional Review Board-approved protocol 13-416.

For BIDMC: The COVID rapid autopsy program was active at BIDMC from April 23, 2020 through May 6, 2020. An email was sent to all physicians caring for COVID patients notifying them about the existence of the program and that participation in the research autopsy program could be offered to families of deceased patients. The decision to offer participation in the autopsy research program to the next of kin of decedents was at the discretion of their treating physicians. In total, five autopsies were performed, representing a small fraction of the patients treated at BIDMC during the initial COVID surge of Spring 2020. No efforts were made to specifically include or exclude subjects based on any demographic data or pre-existing medical condition.

For NYP: Inclusion criteria for autopsies from COVID-19 donors cared for at New York Presbyterian Hospital/Columbia University Medical Center included real-time reverse transcription polymerase chain reaction (RT-PCR) confirmed infection, consent to perform rapid autopsy and post mortem intervals <10 hours. Appropriate consent was obtained from donors or the donors' next of kin. All procedures performed on donor samples were in accordance with the ethical standards of the IRB and the Helsinki Declaration and its later amendments. Frozen control tissues were assessed by a pulmonary pathologist and represent "uninvolved" regions of biobanked tumor resections. Donor characteristics reflect the age, gender, and race representation of patients admitted to New York Presbyterian Hospital/Columbia University Medical Center with COVID-19. Control samples were selected to reflect median age distribution of COVID-19 cases included in the study and match the gender distribution.

#### Ethics oversight

Secondary analysis of samples at the Broad Institute was covered under Massachusetts Institute of Technology (MIT) IRB protocols 1603505962 and 1612793224, or the NHR (not-involving-human-subjects research) protocol ORSP-3635. No subject recruitment or ascertainment was performed as part of the Broad protocol. Samples added to this protocol also underwent IRB review and approval at the institutions where the samples were originally collected. Specifically, Dana-Farber Cancer Institute approved the protocol 13-416, Partners/Massachusetts General Hospital and Brigham and Women's Hospital approved the following protocols: 2020P000804, 2020P000849, 2015P002215; Beth Israel Deaconess approved protocol 2020P000406.224. No subject recruitment or ascertainment was performed as part of the Broad protocol. All tissue specimens of lethal COVID-19 and controls collected at New York Presbyterian Hospital/Columbia University Medical Center were under IRB approved protocols (IRB-AAAT0785 and IRB-AAAB2667). Appropriate consent was obtained from patients or the patients' next of kin. All procedures performed on patient samples at New York Presbyterian Hospital/Columbia University Medical Center were in accordance with the ethical standards of the IRB and the Helsinki Declaration and its later amendments.

Note that full information on the approval of the study protocol must also be provided in the manuscript.